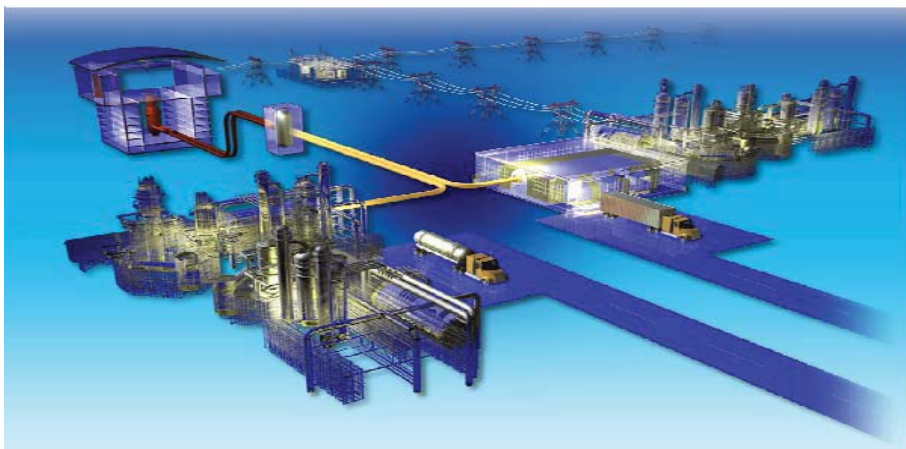


# Insights Gained from Testing Alternate Cell Designs

J. E. O'Brien  
C. M. Stoots  
J. S. Herring  
G. K. Housley  
M. S. Sohal  
D. G. Milobar  
J. J. Hartvigsen  
G. Tao  
N. Petigny  
T. L. Cable

September 2009



The INL is a U.S. Department of Energy National Laboratory operated by Battelle Energy Alliance



# Insights Gained from Testing Alternate Cell Designs

J. E. O'Brien  
C. M. Stoots  
J. S. Herring  
G. K. Housley  
M. S. Sohal  
D. G. Milobar<sup>1</sup>  
J. J. Hartvigsen<sup>2</sup>  
G. Tao<sup>3</sup>  
N. Petigny<sup>4</sup>  
T. L. Cable<sup>5</sup>

<sup>1</sup>University of Arizona

<sup>2</sup>Ceramatec

<sup>3</sup>MSRI

<sup>4</sup>St. Gobain

<sup>5</sup>NASA-Glenn

September 2009

Idaho National Laboratory  
Idaho Falls, Idaho 83415

<http://www.inl.gov>

Prepared for the  
U.S. Department of Energy  
Office of Nuclear Energy  
Under DOE Idaho Operations Office  
Contract DE-AC07-05ID14517

#### **DISCLAIMER**

This information was prepared as an account of work sponsored by an agency of the U.S. Government. Neither the U.S. Government nor any agency thereof, nor any of their employees, makes any warranty, expressed or implied, or assumes any legal liability or responsibility for the accuracy, completeness, or usefulness, of any information, apparatus, product, or process disclosed, or represents that its use would not infringe privately owned rights. References herein to any specific commercial product, process, or service by trade name, trade mark, manufacturer, or otherwise, does not necessarily constitute or imply its endorsement, recommendation, or favoring by the U.S. Government or any agency thereof. The views and opinions of authors expressed herein do not necessarily state or reflect those of the U.S. Government or any agency thereof.




# Insights Gained from Testing Alternate Cell Designs

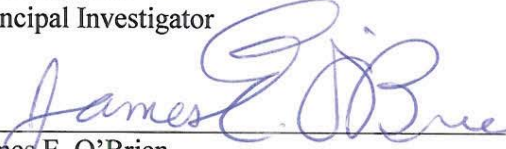
INL/EXT-09-16783  
Revision 0

September 2009

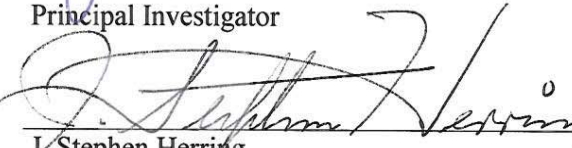
Approved by:

  
\_\_\_\_\_  
Carl M. Stoots  
Principal Investigator

  
\_\_\_\_\_  
Date

  
\_\_\_\_\_  
James E. O'Brien  
Principal Investigator

  
\_\_\_\_\_  
Date

  
\_\_\_\_\_  
J. Stephen Herring  
Technical Director, High Temperature Electrolysis

  
\_\_\_\_\_  
Date



## ABSTRACT

The Idaho National Laboratory (INL) has been researching the application of solid-oxide electrolysis cells for large-scale hydrogen production from steam over a temperature range of 800 to 900°C. The INL has been testing various solid oxide cell designs to characterize their electrolytic performance operating in the electrolysis mode for hydrogen production.

Some results presented in this report were obtained from cells initially developed by the Forschungszentrum Jülich and now manufactured by the French ceramics firm St. Gobain. These cells have an active area of 16 cm<sup>2</sup> per cell. They were initially developed as fuel cells, but are being tested as electrolytic cells in the INL test stands. The electrolysis cells are electrode-supported, with ~10 µm thick yttria-stabilized zirconia (YSZ) electrolytes, ~1400 µm thick nickel-YSZ steam-hydrogen electrodes, and manganite (LSM) air-oxygen electrodes. The experiments were performed over a range of steam inlet mole fractions (0.1 to 0.6), gas flow rates, and current densities (0 to 0.6 A/cm<sup>2</sup>). Steam consumption rates associated with electrolysis were measured directly using inlet and outlet dewpoint instrumentation. On a molar basis, the steam consumption rate is equal to the hydrogen production rate. Cell performance was evaluated by performing DC potential sweeps at 800, 850, and 900°C. The voltage-current characteristics are presented, along with values of area-specific resistance as a function of current density. Long-term cell performance is also assessed to evaluate cell degradation. Details of the custom single-cell test apparatus developed for these experiments are also presented.

NASA, in conjunction with the University of Toledo, has developed another fuel cell concept with the goals of reduced weight and high power density. The NASA cell is structurally symmetrical, with both electrodes supporting the thin electrolyte and containing micro-channels for gas diffusion. This configuration is called a bi-electrode supported cell or BSC. The electrodes are made by freeze-casting, a modified tape-casting technique which creates the many micro-channels in the YSZ electrode green tape. This report presents results of the INL's testing of this new solid oxide cell design as an electrolyzer. Gas composition, operating voltage, and other parameters were varied during testing. Results to date show the NASA cell to be a promising design for both high power-to-weight fuel cell and electrolyzer applications.





# CONTENTS

ABSTRACT.....	v
ACRONYMS.....	xii
NOMENCLATURE .....	xiii
1. INTRODUCTION .....	1
1.1 INL High Temperature Electrolysis Laboratory .....	2
2. SOLID OXIDE CELL AND POLARIZATION LOSSES.....	4
2.1 Solid Oxide Cell.....	4
2.2 Polarization Losses .....	5
3. DEGRADATION PHENOMENA IN SOLID OXIDE ELECTROLYSIS CELLS .....	8
3.1 Degradation Phenomena and Models.....	9
4. PERFORMANCE OF SINGLE ELECTRODE-SUPPORTED CELLS IN THE ELECTROLYSIS MODE .....	12
4.1 Single-Cell Test Apparatus Design and Fabrication.....	12
4.2 Cell Reduction.....	16
4.3 Test Procedure and Analysis.....	16
4.4 Preliminary Test Results .....	18
4.5 Long-Term Performance of St. Gobain Electrode-Supported Cells .....	19
4.6 Post-Test Examination of Electrode-Supported Cells.....	24
5. PERFORMANCE OF THE NASA BI-ELECTRODE SUPPORTED CELL.....	25
5.1 Button Cell Fabrication by NASA .....	25
6. IMPROVED CERAMATEC CELLS .....	33
6.1 Cells Tested at INL .....	33
6.2 Stack fabrication and testing summary for stack tests performed at Ceramatec.....	35
6.3 Button cell fabrication and testing summary for tests performed at Ceramatec. ....	37
6.4 Summary and Future Work - Ceramatec .....	45
7. DEGRADATION STUDIES OF ELECTRODE-SUPPORTED SOLID-OXIDE ELECTROLYSIS CELLS IN A 5-CELL STACK CONFIGURATION AT MSRI.....	46
7.1 Background: .....	46
7.2 Status:.....	46
8. ACKNOWLEDGMENTS .....	56
9. REFERENCES .....	57

## FIGURES

Figure 1-1. Schematic of HTE system coupled to an advanced nuclear reactor.....	1
Figure 1-2. INL high-temperature electrolysis laboratory. ....	2
Figure 1-3. General schematic of one of INL solid oxide cell testing apparatus. ....	3
Figure 2-1. (a) Solid oxide electrolytic cell (SOEC); (b) solid oxide fuel cell (SOFC) (Guan et al. 2006). ....	4
Figure 2-2. SOFC voltage-current characteristics for a single cell operating at 800°C (Windisch et al. 2002). ....	7
Figure 3-1. Operating mechanisms of solid oxide cells: (a) a SOEC in electrolysis mode, and (b) a SOFC in fuel cell mode (Ni et al. 2006). ....	8
Figure 3-2. TPBs in a solid oxide cell, shown as red dots, where reactions take place (Hauch 2007a). ....	11
Figure 4-1. Exploded view of cell test fixture. ....	13
Figure 4-2. (a) alumina cell holder; (b) cell holder with cell in place. ....	13
Figure 4-3. Alumina air flow distributor. ....	14
Figure 4-4. Test stand overview. ....	15
Figure 4-5. Test stand installed in furnace base. ....	15
Figure 4-6. Polarization curves for electrode-supported cell. ....	18
Figure 4-7. Area-specific resistance for electrode-supported cells as a function of current density. ....	19
Figure 4-8 Cell voltage and ASR as a function of current density and operating temperature, initial sweeps, $T_{dpi} = 60^{\circ}\text{C}$ . ....	20
Figure 4-9 Cell voltage and ASR as a function of current density and operating temperature, initial sweeps, $T_{dpi} = 70^{\circ}\text{C}$ . ....	20
Figure 4-10 Dewpoint temperatures and hydrogen production rates as a function of cell current, $T_f = 850^{\circ}\text{C}$ , $T_{dpi} = 68^{\circ}\text{C}$ . ....	21
Figure 4-11 Cell area-specific resistance, long-term durability test. ....	22
Figure 4-12. Cell voltage and current, long-term durability test. ....	22
Figure 4-13. Cell voltage and ASR as a function of current density and cell operation time, $T_{dpi} = 70^{\circ}\text{C}$ . ....	23
Figure 4-14. Closeup of steam/hydrogen electrode after 600-hour test, cell 316-09. ....	24
Figure 4-15. Closeup of oxygen electrode after 600-hour test, cell 316-09. ....	25
Figure 5-1. Cross section of a sintered BSC cell showing the thin YSZ (white) electrolyte in the center and the YSZ scaffolds, and the micro channels (black) formed by the ice crystals during freeze-casting, and then removed during freeze drying. The bright white at the top and bottom of the cell is Au ink. ....	26
Figure 5-2. NASA button cell mounted on support tube. ....	26
Figure 5-3. Polarization curve for first NASA cell tested. ....	27
Figure 5-4. Polarization curve and respective ASR values for NASA cell 3. ....	28

Figure 5-5. Dew points and H <sub>2</sub> production rates for polarization curve in Figure 5-3.....	28
Figure 5-6. Polarization curve and respective ASR values for NASA cell 3.....	29
Figure 5-7. Dew points and H <sub>2</sub> production rates for polarization curve in Figure 5-5.....	29
Figure 5-8. Polarization curve and H <sub>2</sub> production rates for NASA cell 5.....	30
Figure 5-9. Summary of polarization curves for NASA cell 7.....	30
Figure 5-10. Long duration test data for NASA cell 7.....	31
Figure 5-11. Polarization curves for NASA cell 8.....	32
Figure 5-12. Long duration test data for NASA cell 8.....	32
Figure 6-1. Ceramtec stack configuration.....	33
Figure 6-2. Performance of the Ceramtec fully-stabilized electrolyte button cell.....	34
Figure 6-3. Long-term performance (>2500 hrs.), stack 496, tested at Ceramtec.....	36
Figure 6-4. Baseline polarization curves, cell 252.....	38
Figure 6-5 Baseline polarization curves, cell 253.....	39
Figure 6-6. Baseline polarization curves, cell 254.....	39
Figure 6-7. Baseline polarization curves, cell 255.....	40
Figure 6-8. Baseline polarization curves, cell 256.....	40
Figure 6-9. Baseline polarization curves, cell 263.....	41
Figure 6-10. Polarization curves, LPCF cathode, cell 260.....	41
Figure 6-11. Polarization curves, LPCF cathode, cell 266.....	42
Figure 6-12. Long-term test, baseline cell 253.....	42
Figure 6-13 Long-term test, baseline cell 254.....	43
Figure 6-14 Long-term test, baseline cell 255.....	43
Figure 6-15 Long-term test, baseline cell 256.....	44
Figure 6-16 Long-term test, baseline cell 252.....	44
Figure 6-17 Long-term test, LPCF cathode, cell 260.....	45
Figure 7-1. Photograph of 5-cell SOEC stack.....	47
Figure 7-2. Performance characteristics of the M1 5-cell stack tested in the SOFC mode at 800°C. The compositions of the fuel gas were varied from H <sub>2</sub> to 50% H <sub>2</sub> , balance H <sub>2</sub> O.....	47
Figure 7-3. Performance characteristics of the same M1 5-cell stack tested in the SOEC mode at 800°C. The steam concentrations were varied from 90% to 50%. .....	48
Figure 7-4. Long-term test result of the M1 5-cell stack in the SOEC mode at 800°C. The negative electrode gas was 90% H <sub>2</sub> O, balance H <sub>2</sub> .....	48
Figure 7-5. Performance characteristics of the M2 5-cell stack tested in the SOFC mode at 800°C. The compositions of the fuel gas were varied from H <sub>2</sub> to 50% H <sub>2</sub> bal. H <sub>2</sub> O.....	49
Figure 7-6. Performance characteristics of the same M2 5-cell stack tested in the SOEC mode at 800°C. The steam concentrations were varied from 90% to 50%. .....	50

Figure 7-7. Long-term test result of the M2 5-cell stack in the SOEC mode for continuous hydrogen production at 800°C. The negative electrode gas was 70% $\text{H}_2\text{O}$ bal. $\text{H}_2$ .	50
Figure 7-8. M2 5-cell stack functional checks in the SOFC mode at different time. 50% $\text{H}_2$ bal. $\text{N}_2$ was the fuel and air was the oxidant. All tests were performed at 800°C.	51
Figure 7-9. Performance characteristics of the $\text{M2}^+$ 5-cell stack tested in the SOFC mode at 800°C. The compositions of the fuel gas were varied from $\text{H}_2$ to 50% $\text{H}_2$ , balance $\text{H}_2\text{O}$ .	52
Figure 7-10. Performance characteristics of the same $\text{M2}^+$ 5-cell stack tested in the SOEC mode at 800°C. The steam concentrations were varied from 80% to 50%.	53
Figure 7-11. Long-term test result of the $\text{M2}^+$ 5-cell stack in the SOEC mode for a continuous hydrogen production at 800°C. The negative electrode gas was 70% $\text{H}_2\text{O}$ bal. $\text{H}_2$ .	54
Figure 7-12. $\text{M2}^+$ 5-cell stack functional check in the SOFC mode at different time. 50% $\text{H}_2$ bal. $\text{N}_2$ was the fuel, and air was the oxidant. All tests were performed at 800°C.	54
Figure 7-13. Photographs of the test fixture after long-term tests of the second 5-cell stack: (a) before and (b) after moved out of the furnace.	55
Figure 7-14. SEM micrographs of (a) a M1 cell with MSRI standard cell materials; (b) a M2 cell with the advanced cell materials, after long-term tests.	55

## TABLES

Table 2-1. Commonly used materials in SOFC/SOEC (Gazzarri 2007).....	5
Table 4-1. Cell electrode reduction procedure.....	16
Table 5-1. Cell test conditions. ....	27

## ACRONYMS

3-D	three dimensional
ASR	area-specific resistance
CFD	computational fluid dynamics
EDS	energy dispersive X-ray spectroscopy
EIS	electrochemical impedance spectroscopy
HTE	high-temperature electrolysis
ILS	integrated laboratory scale
INL	Idaho National Laboratory
LSC	lanthanum strontium chromite
LSCF	lanthanum strontium cobalt iron oxide
LSF	strontium-doped lanthanum ferrite
LSM	strontium-doped lanthanum manganite
LZO	lanthanum zirconate
Ni-YSZ	nickel-yttria stabilized zirconia
PNNL	Pacific Northwest National Laboratory
ScSZ	scandia-stablized zirconia
SDC	samaria-doped ceria
SEM	scanning electron microscopy
SOEC	solid oxide electrolysis cells
SOFC	solid oxide fuel cell
TEM	transmission electron microscopy
TPB	triple-phase boundary
YSZ	yttria stabilized zirconia

## NOMENCLATURE

$F$	Faraday number, 96487 C/mol
$ASR$	area-specific resistance, $\text{Ohm}\cdot\text{cm}^2$
$\Delta G_f$	Gibbs energy of formation, J/mol
$i$	current density, $\text{A}/\text{cm}^2$
$I$	current, A
$\dot{N}_{H_2}$	molar hydrogen production rate, mol/s
$N_{O_2\text{prod}}$	number of oxygen equivalents
$P$	pressure, kPa
$q''$	heat flux, $\text{W}/\text{cm}^2$
$Q_M$	molar flow rate, mol/s
$Q$	volumetric flow rate, sccm
$R_u$	universal gas constant, J/mol·K
$T$	temperature, K
$T_{dp}$	dewpoint temperature
$U_{H_2O}$	steam utilization, %
$V_N$	Nernst potential, V
$V_{cell}$	cell operating voltage, V
$V_{OC}$	open-cell voltage, V
$V_{tn}$	thermal neutral voltage, V
$y$	mole fraction
$\rho_M$	standard-state molar density, $\text{mol}/\text{m}^3$





# 1. INTRODUCTION

Idaho National Laboratory (INL) is performing high-temperature electrolysis (HTE) research to generate hydrogen using solid oxide electrolysis cells (SOECs). A conceptual schematic depicting a high-temperature gas-cooled reactor coupled to an HTE system is shown in Figure 1-1. This system produces hydrogen using the heat and electricity generated by a high-temperature nuclear reactor. The  $\sim 900^{\circ}\text{C}$  primary helium coolant uses about 85% of the thermal energy output of the reactor to drive a gas-turbine Brayton power cycle, which provides the electrical energy required for the HTE process. The remaining 15% of the reactor thermal energy is used to generate steam at about  $850^{\circ}\text{C}$ . The combination of a high-efficiency power cycle and the direct utilization of nuclear process heat yields an overall thermal-to-hydrogen conversion efficiency of 50% or higher.

The objective of the INL project is to address the technical and scale-up issues associated with the implementation of SOEC technology for hydrogen production from steam. In the envisioned application, HTE would be coupled to an advanced nuclear reactor for efficient, large-scale, non-fossil, non-greenhouse gas hydrogen production. The project supports a broad range of activities, including

small bench-scale experiments, larger-scale technology demonstrations, detailed computational fluid dynamic modeling, and system modeling. For this technology to be successful in a large industrial setting, several issues related to solid oxide cells need to be resolved, including: stack design optimization, identification and evaluation of cell performance degradation parameters and processes, integrity and

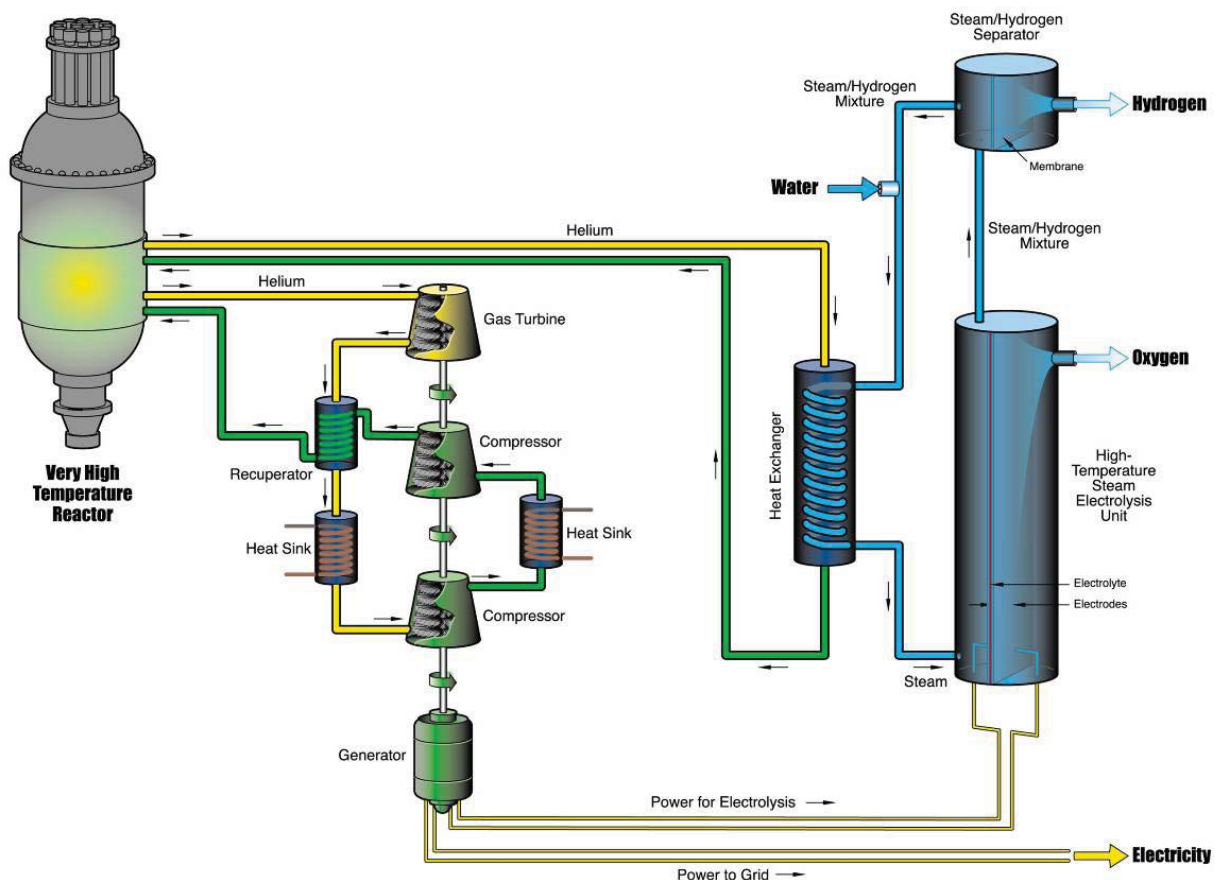


Figure 1-1. Schematic of HTE system coupled to an advanced nuclear reactor.

reliability of the SOEC stacks, lifetime prediction, and extension of the SOEC stacks. This report provides a summary of the cell and stack testing and their degradation characteristics. A part of this report is taken from four previous reports associated with related ongoing work on high temperature electrolysis at INL (Sohal 2009a, Sohal et al. 2009b, Stoots et al. 2009a, Hartvigsen et al. 2009, O'Brien et al. 2009a and 2009b).

## 1.1 INL High Temperature Electrolysis Laboratory

A photograph of the INL HTE laboratory dedicated to small-scale experiments with single cells and small stacks is shown in Figure 1-2. A comprehensive discussion of the INL high temperature solid oxide electrolysis bench-scale experiment is presented elsewhere (Stoots et al. 2009). This same facility is used for button cell testing as well as stack testing. A schematic of the test hardware shown in Figure 1-2 is presented in Figure 1-3. Primary components include: gas supply cylinders, mass-flow controllers, a heated water-bath humidifier, on-line dewpoint sensors, temperature and pressure measurement instruments, high temperature furnace, and the solid oxide electrolysis cell. Nitrogen is used as an inert

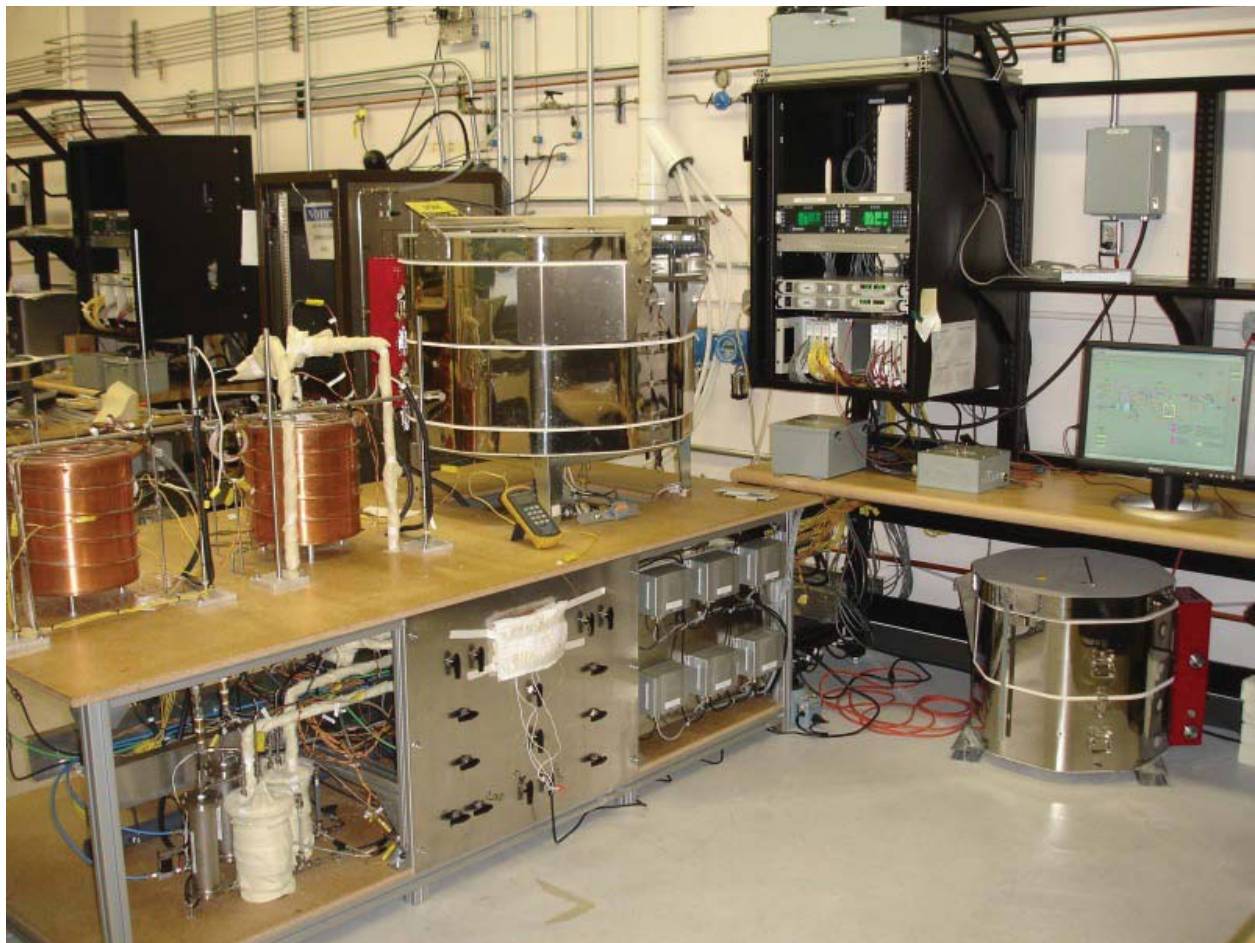


Figure 1-2. INL high-temperature electrolysis laboratory.

carrier gas. The use of a carrier gas allows for independent variation of both the partial pressures and the flow rates of the inlet steam and hydrogen while operating near atmospheric pressure. Inlet flow rates of nitrogen, hydrogen, and air are established by means of precision mass-flow controllers. Hydrogen is included in the inlet flow as a reducing gas in order to prevent oxidation of the Nickel cermet (ceramic-metal) electrode material. Air flow to the stack is supplied by the shop air system, after passing through a two-stage extractor/dryer unit. The cathode-side inlet gas mixture consisting of hydrogen and nitrogen is mixed with steam by means of a heated humidifier. The dewpoint temperature of the nitrogen-hydrogen-steam gas mixture exiting the humidifier is monitored continuously using a precision dewpoint sensor. All gas lines located downstream of the humidifier are heat-traced in order to prevent steam condensation.

Downstream of the mass-flow controllers, nitrogen is mixed with smaller flows of hydrogen gas. Hydrogen is included in the inlet flow as a reducing gas in order to prevent oxidation of the Nickel cermet electrode material. The nitrogen-hydrogen gas mixture is mixed with steam by means of a heated humidifier. The humidifier water temperature is maintained at a constant setpoint value using computerized feedback control. The dewpoint temperature of the nitrogen-hydrogen-steam gas mixture exiting the humidifier is monitored continuously using a precision dewpoint sensor. Pressure is also measured at the dewpoint measurement stations using absolute pressure transducers. Local stream pressure information is required to determine the mole fraction of steam in the gas mixture at the dew point measurement station. Since the nitrogen and hydrogen flow rates are fixed by the mass flow controllers, and the steam partial pressure is fixed by the bath temperature, the complete inlet gas composition is precisely known at all times. All gas lines located downstream of the humidifier are heat-traced in order to prevent steam condensation. Gas line temperatures are monitored by thermocouples and controlled by means of computer-controlled SCRs.

The electrolysis product stream exiting the furnace is directed towards a second dewpoint sensor and then to a condenser through a heat-traced line. The condenser removes most of the residual steam from the exhaust. The final exhaust stream is vented outside the laboratory through the roof. The rate of steam electrolysis is measured via two different, independent methods: (1) electrical current through the stack and (2) the measured change in inlet and outlet steam concentration as measured by the on-line dew-point sensors.

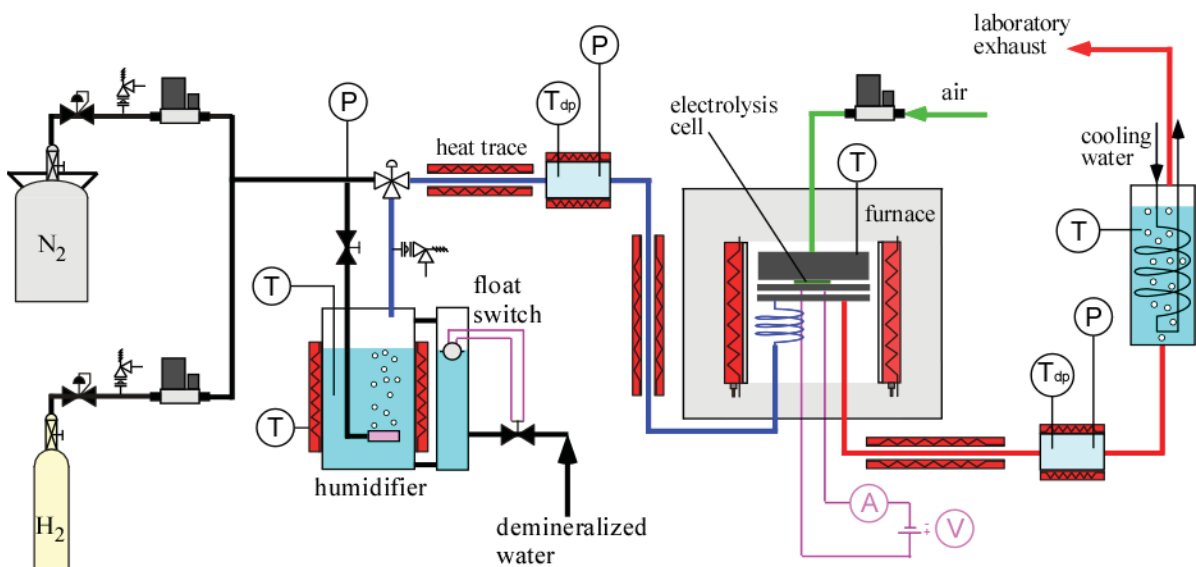


Figure 1-3. General schematic of one of INL solid oxide cell testing apparatus.

Herring et al. (2007) presented the progress of INL HTE research from small-scale bench testing to large-scale demonstration. INL has conducted experiments with following cells/stacks:

- Button cell testing (~1 W)
- Stack testing (200 W–5 kW)—electrode, electrolyte, and interconnect materials, flow channel materials and fabrication, inter-cell electrical contact, cell and manifold sealing issues, and cell durability.
- ILS testing (15 kW)—all previous issues plus multiple-stack thermal management, heat recuperation, feedstock heating, and hydrogen.

## 2. SOLID OXIDE CELL AND POLARIZATION LOSSES

This section provides a general introduction to solid oxide cell construction, material composition, and polarization mechanisms.

### 2.1 Solid Oxide Cell

A solid oxide cell is a key component of the electrolysis system. It consists of three main components: an electrolyte and two electrodes (Figure 2-1). The electrolyte is a ceramic membrane that can conduct ions and is sandwiched between two porous electrodes that can conduct electrons: the steam/hydrogen electrode (commonly called anode in fuel cell mode) and the air/oxygen electrode (cathode in the fuel cell mode). In the fuel cell mode, oxygen molecules dissociate at the oxygen electrode and combine with electrons coming from an external electric power source to form oxygen ions (Figure 2-1b). The oxygen ions conducted through the electrolyte migrate towards the hydrogen electrode. The fuel (hydrogen or natural gas) is fed to the anode and reacts with the oxygen ions to form water and  $\text{CO}_2$ , while the resulting free electrons are transported via the external circuit through the load and back to the oxygen electrode. If the fuel cell is operated in the electrolysis mode (Figure 2-1a), the names and functions of the electrodes get reversed. Thus, the properties of the oxygen electrode should be such that it provides a component for oxygen gas to be easily reduced. Similarly, the function of the hydrogen electrode is to oxidize the fuel gas. The solid oxide electrolyte separates the reduction and oxidation reactions.

The most common materials in use for the solid oxide cells are listed in Table 2-1 (Gazzarri 2007). The electrolyte is a dense gas-tight ceramic layer, usually made from YSZ with a yttria content of 8 mol% to fully stabilize the electrolyte composition. The performance of the electrolyte depends on how well it

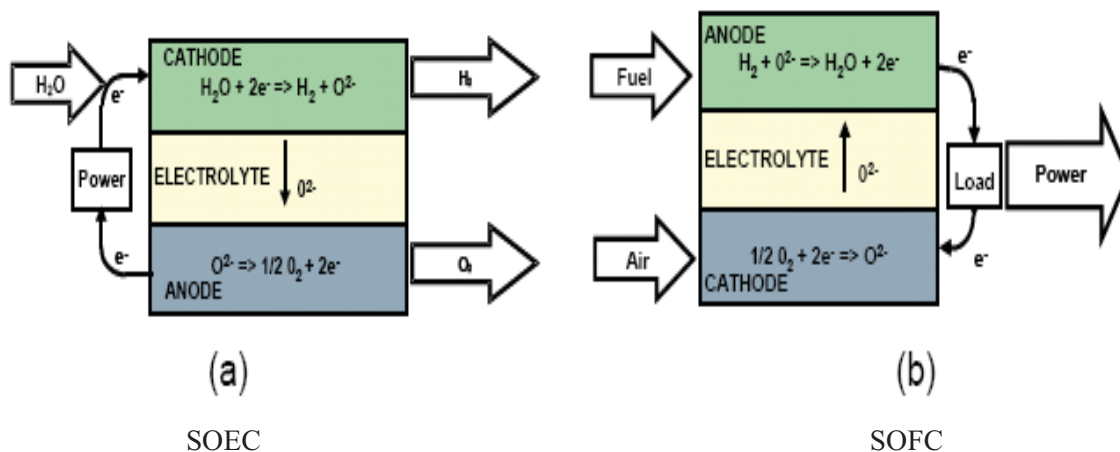


Figure 2-1. (a) Solid oxide electrolytic cell (SOEC); (b) solid oxide fuel cell (SOFC) (Guan et al. 2006).



Table 2-1. Commonly used materials in SOFC/SOEC (Gazzarri 2007).

Component	Material	Acronym
Steam/hydrogen electrode	Ni - Y <sub>x</sub> Zr <sub>1-x</sub> O <sub>2-x/2</sub> (nickel-yttria stabilized zirconia)	Ni-YSZ
Electrolyte	Y <sub>x</sub> Zr <sub>1-x</sub> O <sub>2-x/2</sub> (yttria stabilized zirconia)	YSZ
Air/oxygen electrode	Sr <sub>x</sub> La <sub>1-x</sub> MnO <sub>3-δ</sub> + Y <sub>x</sub> Zr <sub>1-x</sub> O <sub>2-x/2</sub> (doped lanthanum manganite)	LSM-YSZ
Interconnect	Chromium-based alloys/ceramics or stainless steel	SS

can conduct oxide ions (O<sup>2-</sup>). The thinner the electrolyte, the higher its ionic conductance and the lower the cell's ohmic resistance. In an electrolyte-supported cell, the electrolyte thickness is large (150–250 μm), which leads to relatively high ionic resistance. Therefore, if the mechanical strength can be provided by the steam/H<sub>2</sub> electrode, the electrolyte thickness can be reduced by a factor of ~10.

The most common anode material for SOFCs is a porous cermet made from Ni and YSZ. Electronically conductive, gas-tight interconnect plates connect the individual cells to form a stack. Since the electrolyte generally represents the highest resistivity layer in the cell, decreasing its thickness can lead to improved performance. The nickel cermet material (anode in the fuel cell mode, cathode in the electrolysis mode) has relatively high electronic conductivity and is therefore a logical choice for use as the mechanical support layer in electrode-supported cells. The ionic conductivity of ceramics is highly dependent on the ceramic temperature. Thus, high operating temperatures are required to obtain sufficient overall conductivity in the solid oxide cell. YSZ exhibits acceptable conductivity in the 700–1,100°C temperature range, but if thermal cycling occurs, such as at start-up, the high operating temperature results in large thermal stresses in the cell components. Stresses can also be caused by large thermal gradients generated by the uneven distribution of electrochemical reaction sites. Finally, fabrication of the cell components also requires high temperatures that can cause detrimental residual stresses within the cell components. Guan et al. (2006) performed studies for reversible solid oxide cells, which were tested in both fuel cell and electrolysis modes. They selected YSZ (8 mol% Y<sub>2</sub>O<sub>3</sub> doped zirconia) as electrolyte material. Selected oxygen electrodes were strontium-doped lanthanum manganite (LSM), strontium-doped lanthanum ferrite (LSF), and lanthanum strontium cobalt iron oxide (LSCF). They used a samaria-doped ceria (SDC) interlayer for LSF and LSCF. LSCFs have increased ionic conductivity and may reduce the degradation rate in electrolysis mode. For the hydrogen electrode, Ni-YSZ was selected with a varying volume fraction of Ni (40–80%).

In the electrolyzer mode, the electrical energy is used to split hydrogen from steam. The electrolysis process is the reverse of the fuel cell process in which a mixture of steam and hydrogen is fed to the electrolytic cells. The oxygen migrates through the solid-state electrolyte as O<sup>2-</sup> ions because of the imposed voltage. The cell voltage is about 0.4 V lower than that required in conventional electrolyzers because of the high operating temperature.

## 2.2 Polarization Losses

The polarization loss definitions described in this chapter are written strictly for a SOFC. Appropriate care should be applied when applying the same fundamentals for a SOEC case.

When a fuel cell is not connected to an external load, there is no current flow and the maximum reversible cell voltage or open circuit voltage can be calculated by the equilibrium Nernst potential for the specific electrochemical reaction system. The Nernst potential,  $V_{\text{Nerst}}$ , is calculated using the partial pressure of the chemical species at the cell inlet or outlet. However, it is more appropriate to calculate an

average of the inlet and outlet values,  $V_{Nernst}^i$  and  $V_{Nernst}^o$ , where superscripts “i” and “o” represent inlet and outlet locations as

$$V_{Nernst} = \frac{1}{2} (V_{Nernst}^i + V_{Nernst}^o) \quad (1)$$

$$V_{Nernst}^i = -\frac{\Delta G^0}{n_e F} - \frac{RT}{n_e F} \ln \left( \frac{P_{H_2O}^i}{P_{H_2}^i \sqrt{P_{O_2}^i}} \right) \quad (2)$$

$$V_{Nernst}^o = -\frac{\Delta G^0}{n_e F} - \frac{RT}{n_e F} \ln \left( \frac{P_{H_2O}^o}{P_{H_2}^o \sqrt{P_{O_2}^o}} \right) \quad (3)$$

where

$\Delta G^0$  = change in Gibbs free energy at standard conditions and equals  $-RT \ln[K(T)]$

R = universal gas constant

T = cell temperature

K = equilibrium constant

$n_e$  = number of electrons participating in the electrochemical reaction

F = Faraday's constant, and p is the partial pressure of respective species.

When a fuel cell starts supplying electric current to an external load, its operating voltage drops because of irreversibilities associated with internal resistances. The difference between the maximum reversible cell voltage or open circuit voltage ( $V_{OCV}$ ) and the operating cell voltage ( $V_{open}$ ) is termed polarization loss ( $\eta$ ). Cell performance depends on the overall cell reaction and the type of reactants at the electrodes and the reaction product(s). Ivers-Tiffée and Virkar (2003) and Akkaya (2007) give a detailed description of polarization losses. The total polarization loss of an operating cell consists of three dominant parts: activation (or charge transfer) polarization ( $\eta_{act}$ ); concentration (or diffusion) polarization which includes chemical reaction polarization ( $\eta_{conc}$ ); and ohmic resistance polarization ( $\eta_{ohm}$ ).

$$\eta = \eta_{act} + \eta_{conc} + \eta_{ohm} \quad (4)$$

The current efficiency can be stated as the percent of current passing through an electrolytic cell (or electrode) that accomplishes the desired chemical reaction compared to the ideal case. For example, in the hydrogen fuel cell, ideally every hydrogen ( $H_2$ ) molecule would react to produce two electrons that would contribute to the current flow. The inefficiencies arise from reactions other than the intended one taking place at the electrodes or the side reactions consuming the current. Some hydrogen, for instance, may go through the electrolyte and not react at all, or the hydrogen does react but the resulting current is driven through the electrolyte (not the electrode) and never contributes to the current flow.

The voltage efficiency is defined as the net voltage (cell equilibrium voltage minus the irreversible losses) divided by the maximum voltage. The irreversible voltage losses are attributed to polarization losses that primarily originate from three sources: activation, concentration, and ohmic polarizations.

Thus, the net cell voltage is the open circuit voltage minus the various polarization losses and can be written as:

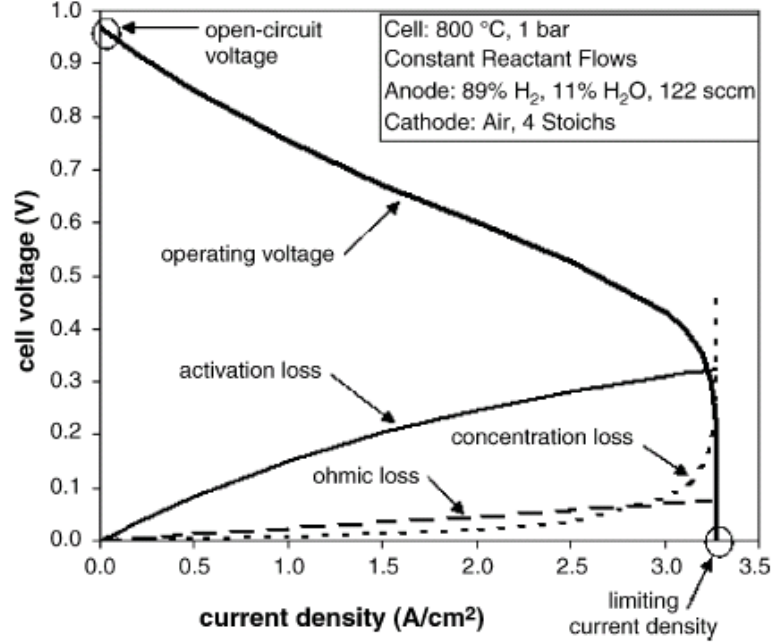


Figure 2-2. SOFC voltage-current characteristics for a single cell operating at 800°C (Windisch et al. 2002).

$$V_{cell} = V_{open} - (V_{act} + V_{conc} + V_{ohm}) = V_{Nernst} - V_{loss} \quad (5)$$

Figure 2-2, developed by Windisch et al. (2002), shows the relative magnitude of various polarization losses in a SOFC. It shows that activation losses are the dominant mode of three types of polarization losses. It also shows the upper limit of current density for the fuel cell to operate.

The overpotentials can be determined by the several models available in the literature—for example, Virkar (2007). However, the concentration overpotentials are different between the SOEC and SOFC modes because of the different gas transport mechanisms in the porous electrodes. Ni et al. (2006) showed that concentration overpotentials are the sole factor responsible for the different current-voltage (i-V) characteristics between the SOEC and SOFC modes. Their analytical model shows the differences in the gas transport mechanisms of the two modes. The selection of an electrode support can greatly affect the overall performance of a reversible solid oxide cell.

A hydrogen-electrode (fuel cell anode) support is favorable for the SOFC mode while an oxygen-electrode (electrolysis anode) support is favorable for the SOEC mode. Therefore, the details of both SOEC and SOFC operating conditions should be carefully considered in their design. If a specified solid oxide cell is mainly used for hydrogen generation, an oxygen-electrode (electrolysis anode) supported cell is recommended. Therefore, corresponding resistance of a SOFC is the cell resistance normalized by its area ( $\text{k}\Omega \cdot \text{cm}^2$ ) and is called area-specific resistance (ASR). From the cell polarization and corresponding current density, an ASR can be defined as

$$ASR = (E - V)/i \quad (6)$$

where

$E$  = either open circuit voltage potential ( $E_{OCV}$ ) or the ideal Nernst potential ( $E_N$ ), depending on whether one wants to (1) remove loss effects due to reactant leakage and variable reactant mixture supply and if one is focused on the cell material performance, or (2) focus on total cell performance (cell material and seals) (Gemmen et al. 2008).

Some methods for reducing this resistance include using:

- Electrodes with high electronic/ionic conductivity
- Appropriate bipolar plate/interconnect materials that are low in ohmic resistance and also complement the other cell component materials
- Thin, but structurally stable electrolyte with the ability to prevent shorting from one electrode to the other.

The important factor to remember about various polarization components is that they are not independent of each other. A change in partial pressure affects the concentration polarization, and it will also affect the activation polarization.

### 3. DEGRADATION PHENOMENA IN SOLID OXIDE ELECTROLYSIS CELLS

As INL progressively increases the scale of electrolyzer systems by increasing the number of solid oxide cells and stacks, it is important to understand and address the causes of performance degradation in SOEC stacks. Unfortunately, not many studies in the published literature address degradation and related issues in SOECs. Even for SOFCs, the issues of degradation, aging, and longevity are topics of ongoing research. As thinner electrolytes with higher ionic conductivity are developed, the overall cell polarization losses are dominated by the electrochemical losses at the anodes and cathodes. Even though the solid oxide cells have several differences while operating in power generating (fuel cell) and electrolysis modes, the degradation mechanisms in the two cases may have some similarities. Therefore, the knowledge of degradation mechanisms in SOFCs can be a starting point for the SOECs and can offer some guidance in identifying the research areas. This being the case, some known degradation background in SOFCs is reviewed here.

Ni et al. (2006) have developed models for concentration overpotential in SOECs and SOFCs, as shown in Figure 3-1(a) and (b), respectively. The cathode (hydrogen electrode) in the electrolysis mode is termed “anode” in the fuel cell mode. Similarly, the anode (oxygen electrode) in the electrolysis mode is termed “cathode” in the fuel cell mode.

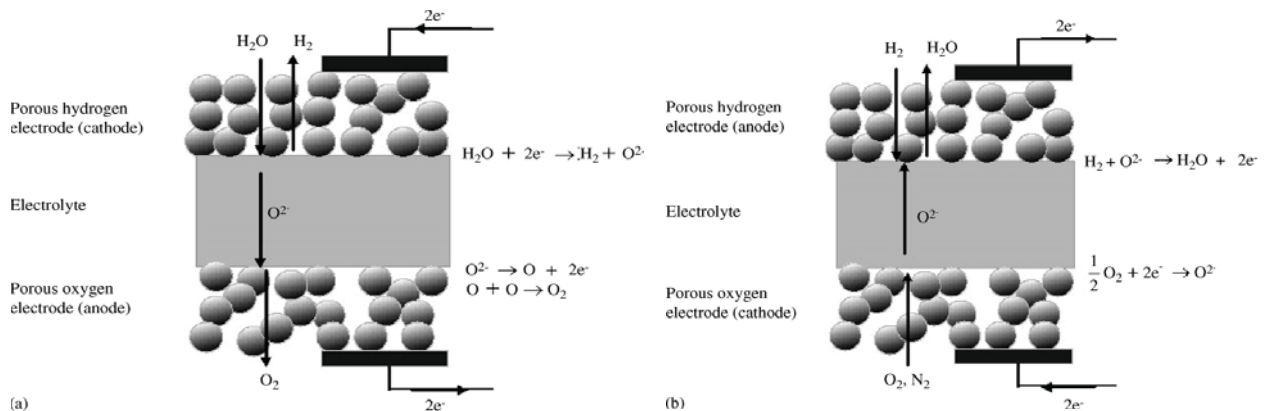


Figure 3-1. Operating mechanisms of solid oxide cells: (a) a SOEC in electrolysis mode, and (b) a SOFC in fuel cell mode (Ni et al. 2006).



### 3.1 Degradation Phenomena and Models

There are two common definitions for quantifying degradation given by Gemmen et al. (2008). The ASR represents an instantaneous performance measure. Another degradation definition is termed “average degradation rate,”  $\overline{DR}(t)$ . It is defined for a time period of  $(t-t_0)$ . Thus, for any cell voltage  $V(I_s, t)$ , at a time  $t$ , average degradation rate,  $\overline{DR}(t)$ , is given by Gemmen et al. (2008) as

$$\overline{DR}(t) = \frac{V(i_s, t_0) - V(i_s, t)}{V(i_s, t_0) \times (t - t_0)} 100. \quad (7)$$

ASR is best suited for comparing the performances of the same cell with two types of technologies, such as one type of interconnect design with another. However, DR is better suited to comparing cell performance with a stack performance of the same type of cells. To understand the degradation phenomena, a solid oxide electrolyzer needs to be operated and tested.

Figure 4-6 and Figure 4-7 show some of the data that were taken during the tests performed at INL. Current density, voltage, ASR, cell system temperature, reactants, and product flow rates are some of the commonly measured parameters during the tests. However, to understand the electrochemical behavior of the electrodes and electrolytes, their chemical microstructure has to be understood before and after an electrolysis operation. Also, the movement of impurities (for example, Ni, Cr) as a result of the electrolysis operation should be identified. The impact of the impurities' movement on electrochemical performance of a single cell and a stack should also be determined by making relevant measurements.

Recently, Virkar (2007) developed an overpotential model for a typical planar SOFC stack comprising several cells connected in series. He also gave the following argument in favor of developing a fundamental understanding of the degradation. In a stack, cell-to-cell characteristics should be as uniform as possible so that, at a given operating current, the voltage across each cell is essentially the same. If, because of some structural/fabrication flaws, the cells are not identical, the resistance and voltage drop will vary from cell to cell. In such a case, the remainder of the cells in the stack will drive the cell with higher resistance. In an extreme case, for the stack to continue operating, the voltage across a cell with higher resistance can even become negative, which can eventually lead to cell failure and increased local temperatures. This phenomenon can spread to adjacent cells in a domino effect.

However, interpretation solely based on visual observations, without a sound theoretical basis for all the phenomena occurring in a cell, may be misleading. In a cell, observations are the aftermath result of some other critical damage to the cell that has already taken place, so the visual observation alone may not be able to show the root cause of the problem. Some of the likely reasons of cell degradation include small initial compositional inhomogeneities resulting in large changes in properties, the formation of local hot spots leading to local changes in microstructures and material properties, electrode delamination due to thermal cycling/rapid heating, reaction between electrode and electrolyte forming a high-resistance layer, fuel and/or oxidant maldistribution, nonuniform oxidation of the interconnect, degradation of the seals, etc. In a normal SOFC, the direction of the (oxygen) ionic current is opposite to that of electronic current. However, if a cell has degraded to cause negative voltage, the direction of electron flow will reverse and both ionic and electronic currents will flow in the same direction.

Virkar (2007) developed a degradation model based on this premise; that is, a cell with higher resistance compared to the rest of the cells in the stack and operating under a negative voltage will be prone to degradation. Planar stacks are more likely to undergo such a degradation mechanism than tubular stacks. Therefore, the ability to measure voltage across each (planar) cell could help in preventing catastrophic failure by either performing preventive maintenance or shorting the bad cell. A similar

degradation model of a SOEC can also offer some insight into the cell degradation phenomenon during the electrolysis mode.

According to Virkar (2007), one of the principal modes of failure of solid-state electrolytes is related to the generation of high chemical potentials and corresponding ultra-high pressure of neutral species within the electrolyte. For example, in an oxygen ion conducting solid electrolyte such as YSZ, under some thermodynamic conditions, oxygen chemical potential within the solid electrolyte,  $\mu_{O_2}^{YSZ}$ , may exceed the chemical potential of gaseous oxygen, that is, under certain conditions,

$\mu_{O_2}^{YSZ} > \mu_{O_2}^{O_2 \text{ electrode}}$ . The chemical potential of any reactant is a function of its partial pressure,

$\mu_{O_2} = f(p_{O_2})$ . Therefore, under certain conditions,  $p_{O_2}^{YSZ} > p_{O_2}^{O_2 \text{ electrode}}$ ; and in some cases,

$p_{O_2}^{YSZ} \gg p_{O_2}^{O_2 \text{ electrode}}$ . If very high pressure develops, it may result in electrode delamination. This increases the cell resistance and then degradation propagates.

Under the same operating conditions of temperature and current density, a SOFC and a SOEC are likely to have the same ohmic and activation overpotentials. Over the past few years, extensive research has been performed relating to SOFC. Yet SOFCs have not reached their complete commercial success because of problems relating to their degradation, longevity, and cost. Some of the degradation mechanisms include contact problems between adjacent cell components, microstructural deterioration (coarsening) of the porous electrodes, and blocking of the reaction sites within the electrodes. Contact problems include delamination of an electrode from the electrolyte, growth of an electronically poorly conducting oxide layer between the metallic interconnect plates and the electrodes, and lack of contact between the interconnect and the electrode. Examples of microstructural degradation are oxygen electrode sintering, carbon deposition, and sulfur or chromium poisoning.

Delamination caused by thermal cycling increases ohmic resistance proportional to the delaminated area. The delaminated area also becomes inactive for electrochemical transport of ions across the electrode and the electrolyte. Chromium-based interconnect oxidation is another important mode that contributes to reducing electrical conductivity between the electrode and interconnect. Sometimes ceramic coatings are used to slow down the rate of oxidation and reduce the rate of chromia evaporation from the interconnects. It was also shown that the loss of performance resulting from interconnect detachment is less severe than that caused by electrode delamination because blocked transport of electrons can now easily move laterally in the electrodes as compared to ions being able to move within the electrolyte. The modeling exercise indicated that results of delamination are highly dependent on the inaccuracies in the knowledge of various cell parameters.

The severe temperature and electrochemical conditions in a solid oxide cell create the need for special materials and pose important challenges to the longevity of the different cell components. The requirements of a solid oxide cell are to facilitate chemical reactions and remove reaction products with the lowest possible resistance. Therefore, the density of reaction sites (sites per unit cell area) and transport paths in a cell should be maximized. For a solid oxide cell to be commercially viable, it should have a 40,000–50,000-hour lifetime. In order to facilitate such a long life, the degradation rate must be very low in all components of the cell stack. It is therefore important to have a fundamental understanding of the degradation mechanism for each component. During operation, any change in the cell that causes blocked reaction sites or transport paths for species will increase the overall cell resistance and thereby the degradation.

One important term used for describing reactions at both electrodes is the so-called triple-phase boundary (TPB). The TPB describes a site in the electrode where the electrochemical reaction takes place, shown as red dots in Figure 3-2 (Hauch 2007a). At the steam/H<sub>2</sub> electrode, this site is where all three

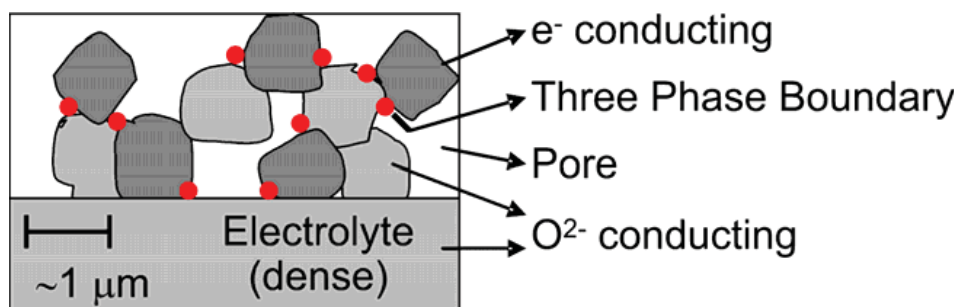


Figure 3-2. TPBs in a solid oxide cell, shown as red dots, where reactions take place (Hauch 2007a).

phases (Ni, YSZ, and gas) are in contact with one other. Since the supply of oxygen ions in the YSZ, the supply of gas in the pores, and the means for transporting the electrons away in the Ni are simultaneously required, the electrochemical reactions are facilitated at the TPB. Therefore, in order to optimize the electrode performance, it is important to maximize the electrochemical activity at the TPBs. For a reaction to take place at the TPB, the gas stream must flow through the pores, Ni must be connected to the interconnect plate, and the YSZ must be connected to the electrolyte either directly or via YSZ in the electrode. Changes in the electrode-electrolyte interfaces and grain boundaries are highly influential in the degradation of the cell. These interfaces not only provide the TPB, but are also active for mass transfer, diffusion, and segregation of species involved in the fuel cell reactions during operation. Microstructural changes in the interfacial regions, such as impurity segregation, will also affect the cell's performance.

The problem of cell degradation also depends on the cell's operating conditions, such as operating temperature, because of increased atomic activity at higher temperatures. It has also been shown that the overall degradation in the cell voltage is more closely correlated to the polarization than to the current density. At high polarization and/or low temperatures ( $\sim 750^{\circ}\text{C}$ ), the oxygen electrode (fuel cell cathode) degradation can be dominant. However, at low polarizations and/or higher temperatures, both electrodes contribute equally to the cell's degradation. From the impedance measurement, it is difficult to assign any degradation phenomenon responsible for overall cell degradation, which implies the importance of correlating electrical measurements with cell microstructural changes.

The mismatch in thermal expansion characteristics of the cell's different layers is a major cause of stresses during thermal cycling occurring during fabrication and operation. In addition, the nonequilibrium chemical reactions throughout the cell also generate large thermal gradients, which in turn generate thermal stresses. These thermomechanical phenomena cause the degradation of the contact between adjacent cell components, namely, the electrolyte-electrode and/or the interconnect-electrode interfaces. This degradation can lead to detachment of two adjacent layers, which results in reduced conductive paths available for electronic transport.

Another example of a degradation mechanism affecting SOFCs is the growth of an electrically insulating oxide layer between the interconnect plate and the electrodes, especially the fuel cell cathode. This leads to an increase in the cell ohmic resistance along the conductive path. The high temperature of operation promotes the kinetics of chromium oxide growth on the stainless steel interconnect plate. Extended periods of operation at high temperature and exposure to contaminants in the reactants also cause microstructural degradation. The electrochemical reactions in SOFCs are not restricted to the interface with the electrolyte, but take place within a few to tens of microns into the volume of the electrode. Therefore, a suitable electrode microstructure is of great importance in providing active surface area at the TPB for electrochemical reaction and sufficient porosity for gas species transport. Consequently, degradation mechanisms that affect electrode microstructure can compromise the cell's performance, stability, and durability.

## 4. PERFORMANCE OF SINGLE ELECTRODE-SUPPORTED CELLS IN THE ELECTROLYSIS MODE

This chapter describes the performance of single electrode-supported cells operating in the electrolysis mode. These cells were originally developed by the Forschungszentrum Jülich as fuel cells and are now being manufactured by the French ceramics firm St. Gobain. In the fuel-cell mode of operation, anode-supported cells represent the state-of-the-art in terms of performance. In an anode-supported SOFC, the anode is typically 1–1.5 mm in thickness while the electrolyte thickness can be as low as 10  $\mu\text{m}$ . In the electrolysis mode, it may be preferable to use an oxygen-electrode-supported cell. A detailed overview of the apparatus that was developed for testing single electrode-supported cells in the electrolysis mode is described in this section, and preliminary test results are provided.

### 4.1 Single-Cell Test Apparatus Design and Fabrication

The test fixture and test stand was designed to evaluate the performance of individual cells without the complicating effects of interconnects. A modified version of this test fixture could be used to test individual cells plus interconnects.

Referring to the exploded view provided in Figure 4-1, a steam / hydrogen mixture enters through a 1/4-in inconel coiled tube into the inlet hole in the bottom of the Hastelloy-X (HastX) base plate. It then flows through a diverging flow channel milled into the HastX base plate and passes through a slot in the bottom of the alumina cell holder. The slots can be seen in Figure 4-2. An alumina felt gasket is used to seal the HastX base plate against the alumina cell holder. The flow then passes under the cell through a corrugated/perforated nickel flow channel (flow field). The flow field establishes the gap for the steam-hydrogen flow channel under the cell while also serving as an electrical conductor. A 0.010-in nickel foil underneath the flow channel serves as a current collector. The Ni foil, flow channel, and mesh are sized to fit into the inner square recess machined into the alumina cell holder. The cell holder and air flow distributor material is fabricated from alumina in order to minimize the potential for chromium poisoning of the cell electrodes. The cell holder was machined in the bisque state and then fired. During firing, the bisque alumina shrinks by about 15%. This shrinkage must be taken into account when doing the machining such that the desired dimensions are achieved in the final dense alumina part.

Electrical contact with the electrodes is accomplished using a gold mesh on the air-side and a nickel mesh on the steam-hydrogen side. A gold wire in direct contact with the nickel foil serves as the steam-hydrogen side power lead and voltage tap. The wire just fits in one of the grooves of the flow channel. The two ends of this wire are fed out through the two small holes shown in the bottom of the alumina cell holder, visible in Figure 4-2(a). After passing along the bottom of the cell, the steam-hydrogen flow exits the alumina cell holder through a second slot and flows through a converging passage in the HastX base plate and out through an 3/8-in OD inconel outlet tube. The outlet tube is sized larger than the inlet tube in order to minimize back pressure on the cell seals to prevent leakage.

The cell is placed on a shelf milled into the alumina cell holder just above and in contact with the Ni mesh (Figure 4-2(b)). The cell dimensions are  $50 \times 50 \times 1.5$  mm (thickness). A nickel paste was used to enhance electrical contact between the cell and the nickel mesh, flow field, and foil. To help with sealing, an alumina felt gasket is placed on the shelf underneath the cell and an alumina-based ceramic paste (Aremco Products, Ceramabond 552) is distributed around the top outer edge of the cell to seal the gap between the cell and the alumina cell holder.

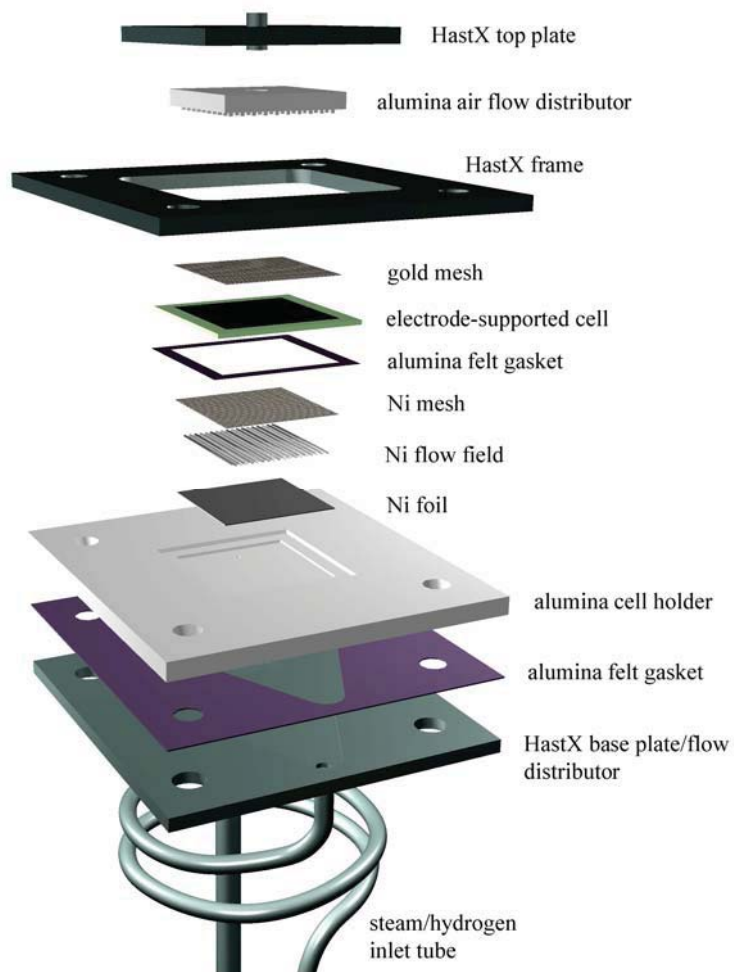


Figure 4-1. Exploded view of cell test fixture.



Figure 4-2. (a) alumina cell holder; (b) cell holder with cell in place.



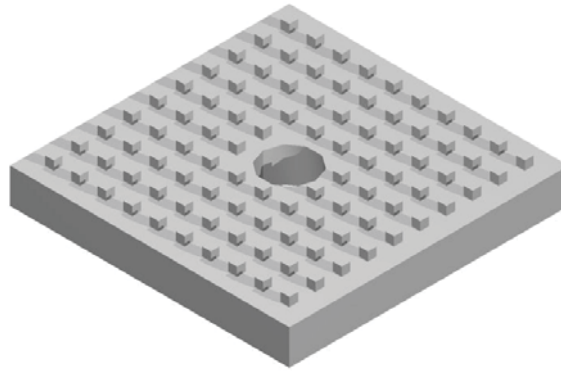


Figure 4-3. Alumina air flow distributor.

A gold mesh contacts the oxygen electrode on the oxygen side of the cell. This gold mesh is held against the oxygen electrode by the alumina air flow distributor. The air flow distributor has an array of square protuberances milled into its surface (Figure 4-3), creating a gap for air flow while also compressing the gold mesh against the air-side electrode. A gold wire is positioned in one of the grooves, in contact with the gold mesh, for current collection. One end of this wire is used as a power lead and the other end is used as a voltage tap.

Air is introduced to the top side of the cell through an inlet tube welded to the HastX top plate. This tube protrudes slightly into a central hole in the alumina air flow distributor. A seal was formed between the HastX top plate and the alumina air flow distributor by means of an alumina felt gasket and a ceramic paste. After exiting the central hole in the air flow distributor, the air impinges on the cathode side of the cell and flows radially outward through the array of protuberances. The air then exits into the furnace volume.

A fixed compressive load is applied to the entire cell stack between the alumina cell holder and the HastX top plate by means of weights, as shown in the test stand overview diagram (Figure 4-4). This load simultaneously compresses the cell against the nickel mesh, flow channel (flow field) and foil on the bottom steam/hydrogen side of the cell and against the gold mesh on the air/oxygen side. It also compresses the cell against the seal around the outer edge of the cell, which rests on the shelf milled into the alumina cell holder. The HastX weight plates are held in alignment by the upper portion of the threaded rods which extend upward for this purpose.

A fixed compressive load is independently applied between the HastX frame, the alumina cell holder, and the HastX base plate. This load is generated by the compression of four springs located under the test stand base support outside of the furnace. The springs will be compressed a fixed amount that is determined by the height of the spool pieces by tightening a nut on the threaded rods. The threaded rods are fed through the alumina spacer tubes. These spacer tubes determine the height of the cell holder inside the furnace. The spring-generated load is intended to compress the seal between the cell holder and the base plate. This seal was formed by alumina felt impregnated with alumina slurry. A nut is visible on the threaded rods in Figure 4-4 just above the HastX frame and below the weight plates. This nut represents the upper stop for this compressive load. The extension of the threaded rods above the nuts is for the purpose of aligning the weight plates. Note that the weight plates are floating above these nuts since they are resting on the HastX top plate.

A photograph of the test stand installed in the furnace base is provided in Figure 4-5. Note that the base support is located outside of the furnace. Holes were drilled in the bottom of the kiln for pass-through of the flow tubes, alumina spacer rods, power leads, and instrumentation.

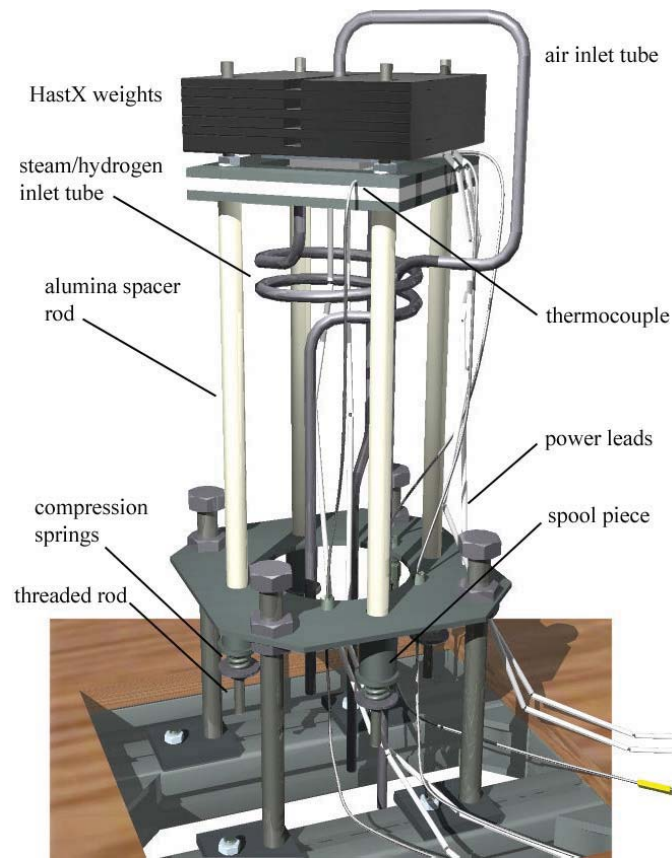


Figure 4-4. Test stand overview.



Figure 4-5. Test stand installed in furnace base.

## 4.2 Cell Reduction

The electrode-supported cells tested in this study are supported by the porous 1.5 mm thick steam-hydrogen electrode whose initial composition is nickel oxide and YSZ. The nickel oxide must be reduced to nickel metal in order for the electrode to become electronically conductive. This reduction process is accomplished by exposing the electrode to increasing levels of hydrogen gas at 900°C, as indicated in Table 4-1. The initial heatup of the cell (step 0) is performed under inert gas at a heatup rate of 1°C/min to 900°C. The cell is then exposed to varying nitrogen-hydrogen-steam gas mixtures for the time durations indicated in the table. The steam was introduced by bubbling the nitrogen-hydrogen gas mixture through a room-temperature water bath (humidifier). The corresponding steam flow rates can be calculated based on the nitrogen and hydrogen flow rates and the bath temperature. These calculated steam flow rate values are listed in the table. The steam/hydrogen electrode of the reduced cell is silver/gray in color.

Table 4-1. Cell electrode reduction procedure.

step	Hold time (min)	H <sub>2</sub> Flow rate (sccm)	T <sub>dp</sub> (°C)	H <sub>2</sub> O flow rate (sccm)	N <sub>2</sub> flow rate (sccm)	Air flow rate (sccm)	T <sub>cell</sub> (°C)	y <sub>H2O</sub>
0 (heatup)	n/a	0	bypass	0	500	500	1°C/min	0
1	75	80	bypass	0	500	580	900	0
2	7.5	160	bypass	0	500	660	900	0
3	7.5	160	22	20.8	500	660	900	0.031
4	5	320	22	25.9	500	820	900	0.031
5	5	500	22	23.7	250	750	900	0.031
6	5	500	22	15.8	0	500	900	0.031

## 4.3 Test Procedure and Analysis

This section describes how test conditions are to be determined. The nominal active area for the cells in this study is 16 cm<sup>2</sup>. The maximum current density is usually set such that the maximum cell voltage is near the thermal neutral voltage ( $V_m = 1.287$  V at 800°C). Once the current density and cell area are known, the total cell current is known ( $I = i \times A_{cell}$ ) and the molar hydrogen production rate can be determined directly from Faraday's law:

$$Q_{M,H_2,prod} = \frac{I}{2F} \quad (8)$$

This molar value can be converted to a standard volumetric flow rate (e.g., sccm) by dividing it by the standard-state molar density,  $\rho_M = 44.615$  mol/m<sup>3</sup>.

A desired value for maximum fraction of steam utilization can then be specified. Depending on the objective of the test, this value could range from 0.2–0.9. Low values of steam utilization generally yield better cell performance in the electrolysis mode. High values can cause localized steam starvation and result in lower cell performance. Analysis of large-scale systems has indicated that overall system performance drops off for steam utilization values below ~0.5, but is fairly flat above that value (O'Brien et al. 2009b). Once the desired steam utilization is specified, the required inlet steam flow rate can be determined from

$$Q_{H_2O,i} = \frac{Q_{H_2,prod}}{U_{H_2O}} \quad (9)$$



Since steam is introduced (in this case) using a humidifier, the steam flow rate depends on both the inlet dew-point temperature, which is approximately the same as the humidifier bath temperature, and the flow rates of nitrogen and hydrogen. So the inlet dew-point temperature must be specified. We typically use a value of 50–70°C for single-cell testing.

For testing in the electrolysis mode, a reasonably high inlet dew-point temperature is required, typically 60–70°C. Once the inlet dew-point temperature is specified, the corresponding inlet mole fraction of steam is given by

$$y_{H_2O,i} = \frac{P_{sat}(T_{dpi})}{P_T} \quad (10)$$

where  $P_{sat}(T_{dpi})$  is the vapor pressure of steam at the specified inlet dew-point temperature, obtained from an appropriate correlation such as the Antoine equation. The total required gas flow of nitrogen plus hydrogen can then be obtained from

$$Q_{gas,i} = Q_{H_2O,i} \frac{1 - y_{H_2O,i}}{y_{H_2O,i}} \quad (11)$$

The inlet flow rate of hydrogen can be determined by specifying the desired inlet mole fraction of hydrogen, typically 0.1–0.2. Inlet hydrogen is required to maintain reducing conditions on the nickel cermet material. The respective flow rates of hydrogen and nitrogen are then obtained from

$$Q_{H_2,i} = \frac{y_{H_2,i}}{y_{H_2O,i}} Q_{H_2O,i} \quad \text{and} \quad (12)$$

$$Q_{N_2} = Q_{gas} - Q_{H_2,i} \quad (13)$$

Air is typically used on the oxygen side of the cell as a sweep gas in order to prevent buildup of pure oxygen. The flow rate of air is scaled with respect to the oxygen production rate,

$$Q_{O_2,prod} = Q_{H_2,prod} / 2 \quad (14)$$

as follows:

$$Q_{air} = \frac{N_{O_2prod} Q_{O_2,prod}}{y_{O_2,air}} \quad (15)$$

where  $N_{O_2prod}$  is a factor indicating the number of oxygen production equivalents desired in the sweep air and  $y_{O_2,air}$  is the mole fraction of oxygen in the sweep gas ( $y_{O_2,air} = 0.21$ ). Typically,  $N_{O_2prod} = 1$ , which yields an outlet sweep gas mole fraction of oxygen equal to 0.347.

Once the cell operating temperature is selected (typically 800°C), the test conditions are fully specified.

## 4.4 Preliminary Test Results

The first indication of cell performance that can be observed is the open-cell potential, which can be calculated using the Nernst equation as given in Equations (2) and (3): Generally, for single-cell testing, if the observed open-cell potential is different from the theoretical value by more than a few millivolts, it points to a possible problem with the cell such as gas leakage, a cracked cell, or a short circuit. Open-cell potentials observed for the cells tested in this study were all within 2 mV of the theoretical value.

Initial electrolysis performance of these cells was evaluated by acquiring data for voltage-current polarization curves at three different operating temperatures. Polarization curves for cell 316-09 are presented in Figure 4-6 as cell voltage versus current density. The inlet gas flow rates and dewpoint temperature used during these sweeps are indicated in the figure. The sweeps were performed by varying the applied cell operating voltage from a value just below the open-cell voltage to a value of 1.3 V, which is just above the thermal neutral voltage. Current densities at 1.3 V were 0.456, 0.553, and 0.613 A/cm<sup>2</sup> at 800, 850, and 900°C, respectively. Negative values of current density in Figure 4-6 correspond to the fuel cell mode of operation and positive values represent the electrolysis mode. The polarization curves are linear through the zero-current transition from fuel-cell mode to electrolysis mode, indicating that activation does not contribute significantly to the observed overpotentials. Cell voltage increases nearly linearly at low current density, but at an increasingly higher rate at higher current densities. The nonlinear behavior at high current density is due to concentration overpotential associated with steam consumption.

Area-specific resistance (ASR) values for this cell are plotted in Figure 4-7 as a function of current density. These “apparent” ASR values are defined by (similar to that defined in Equation (6))

$$ASR = \frac{V_{cell} - V_{OC}}{i} \quad (16)$$

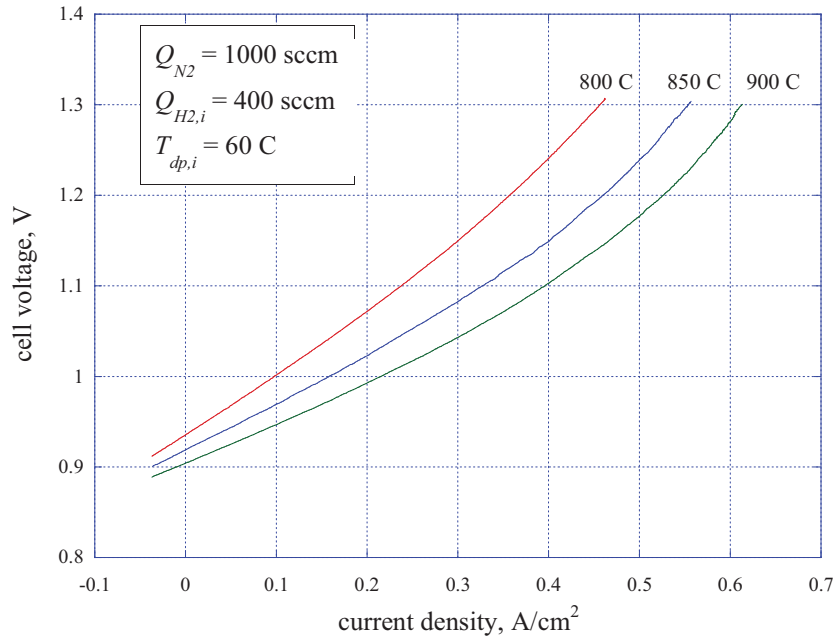


Figure 4-6. Polarization curves for electrode-supported cell.

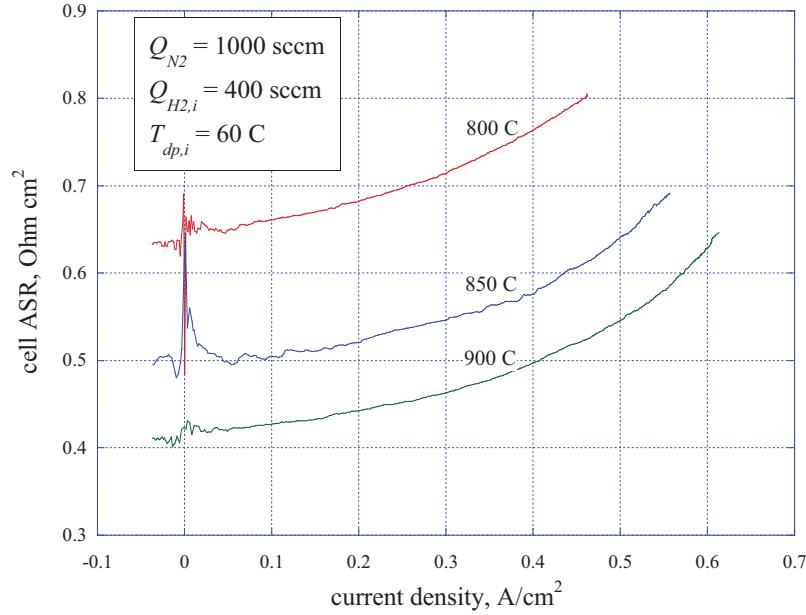


Figure 4-7. Area-specific resistance for electrode-supported cells as a function of current density.

Low-current-density *ASR* values are approximately 0.65, 0.50, and 0.42  $\text{Ohm}\cdot\text{cm}^2$  at 800, 850, and 900°C, respectively. The apparent *ASR* values increase significantly with current density, again reflecting the effect of steam consumption. These initial *ASR* values are quite good, as low as have been observed with the highest performing electrolyte-supported button cells tested at INL.

## 4.5 Long-Term Performance of St. Gobain Electrode-Supported Cells

Long-term durability testing was also performed with St. Gobain cell 316-03. The long-term testing was preceded by initial characterization. Results of the initial sweeps are presented in Figure 4-8 and Figure 4-9. The initial sweeps were performed at 800, 850, and 900°C with humidifier bath temperatures of 60 and 70°C. Each figure shows both a series the *V-i* polarization curves and a series of *ASR-i* curves. The voltage-current density curves are nonlinear, curving upward at high values of current density, revealing the effects of steam starvation and mass transfer through the thick (1.5 mm) steam-side electrode. This effect is more noticeable in the lower dewpoint data of Figure 4-8 than in Figure 4-9.

Cell area-specific resistance values decrease with increasing operating temperature and increasing steam content. The apparent *ASR* values presented in Figure 4-8 than in Figure 4-9 are calculated from Eqn (16). Initial low-current *ASR* values for the 60°C inlet dewpoint sweeps were 0.62, 0.52, and 0.48  $\text{Ohm}\cdot\text{cm}^2$  at 800, 850, and 900°C, respectively. These values are very similar to the *ASR* values observed with cell 316-02. Corresponding values for the 70°C inlet dewpoint sweeps were 0.57, 0.48, and 0.41  $\text{Ohm}\cdot\text{cm}^2$ .

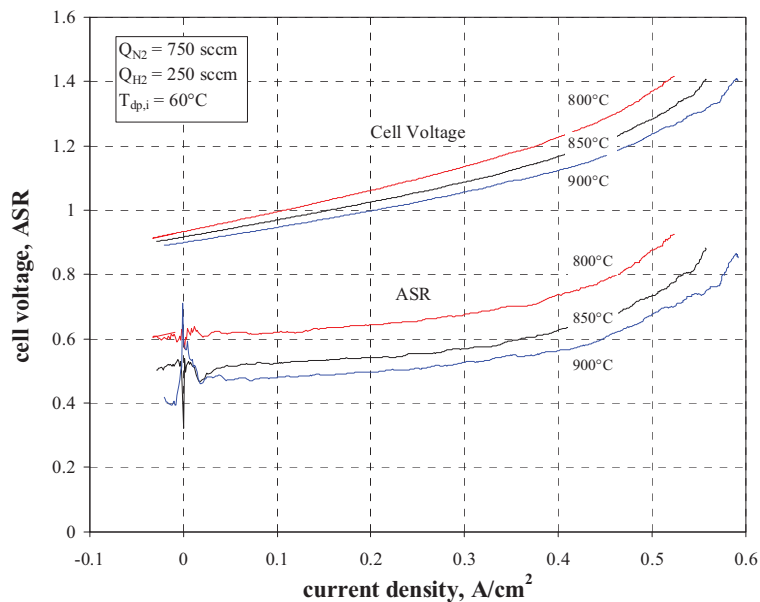


Figure 4-8 Cell voltage and ASR as a function of current density and operating temperature, initial sweeps,  $T_{dp,i} = 60^\circ\text{C}$ .

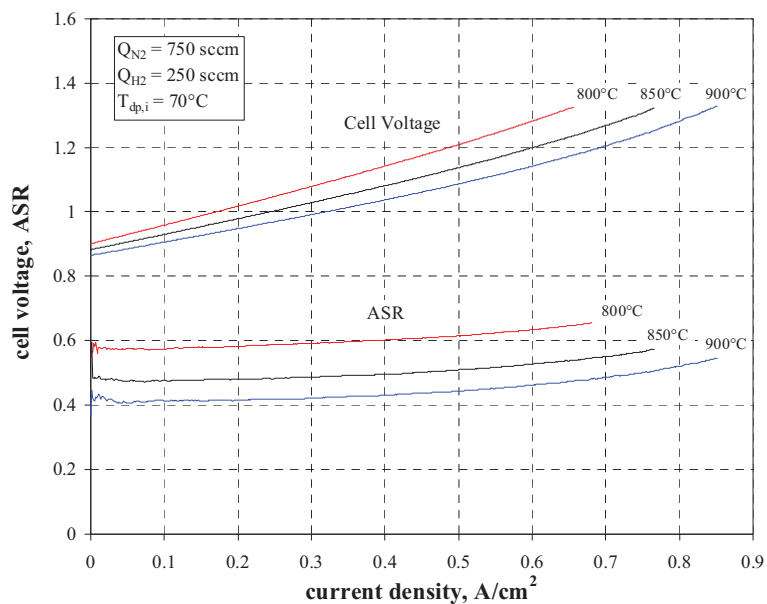


Figure 4-9 Cell voltage and ASR as a function of current density and operating temperature, initial sweeps,  $T_{dp,i} = 70^\circ\text{C}$ .

Hydrogen production rates during cell operation can be calculated based on cell current using Faraday's law. In addition, hydrogen production rates can be determined independently based on inlet and outlet dewpoint measurements. These measurements provide a direct indication of steam consumption rate, which on a molar basis is equal to the hydrogen production rate. Representative plots of inlet and outlet dewpoint temperatures and hydrogen production rates measured during a sweep are presented in Figure 4-10. In this figure, the inlet dewpoint temperature is essentially constant, as expected, with a value of 67.2°C. The outlet dewpoint temperature decreases with increasing cell current, due to conversion of steam to hydrogen. Hydrogen production rates are also presented in the figure in standard cubic centimeters per minute (sccm). The straight black line represents the hydrogen production rate based on cell current, using Faraday's law. The green line represents the hydrogen production rate base on the inlet and outlet dewpoint temperatures. This line naturally includes some scatter, but the agreement between the two independent measurements of hydrogen production rates is generally quite good, providing confidence in the experimental results.

Long-term operation of this cell was initiated on July 17, 2009. This cell was subsequently operated for over 600 hours at 850°C. During the first 250 hrs. of operation, the cell was operated at a voltage of 1.21 V, with a nominal inlet dewpoint value of 60°C. At this time, a series of sweeps was performed for comparison to the initial sweeps. These sweeps were performed at both 60 and 70°C inlet dewpoint temperatures. Subsequently, the long-term durability test was continued, retaining the higher inlet dewpoint value of 70°C. At an elapsed time of 590 hrs, a final sweep was performed.

Results of long-term durability testing for this cell are presented in Figure 4-11 through Figure 4-13. Figure 4-11 Cell area-specific resistance, long-term durability test. shows the time history of cell voltage and current over 590 hours of elapsed test time. There is a step change in voltage and current at ~260 hours, associated with an increase in the humidifier bath temperature from 60 to 70°C. This change in inlet steam content yielded a lower cell ASR value, resulting in a lower open-cell voltage, and a higher cell current at the same operating voltage.

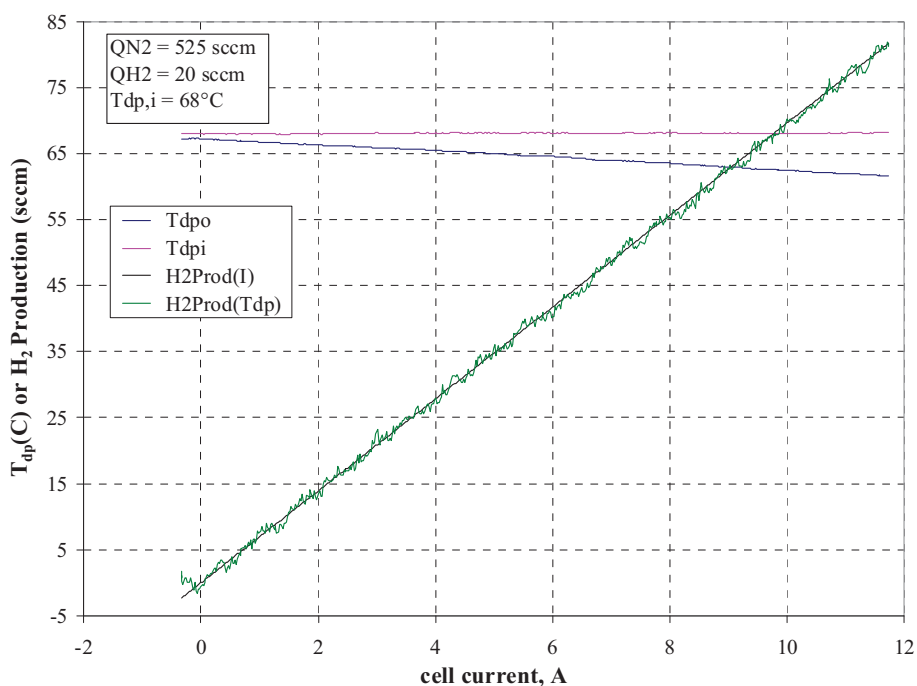


Figure 4-10 Dewpoint temperatures and hydrogen production rates as a function of cell current,  $T_f = 850^\circ\text{C}$ ,  $T_{dpi} = 68^\circ\text{C}$ .

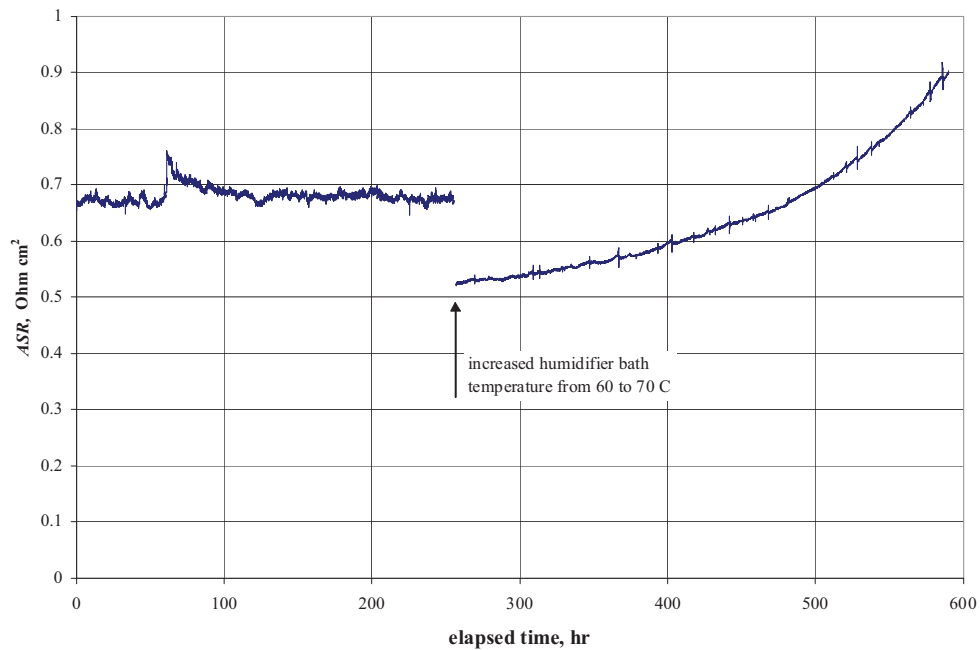


Figure 4-11 Cell area-specific resistance, long-term durability test.

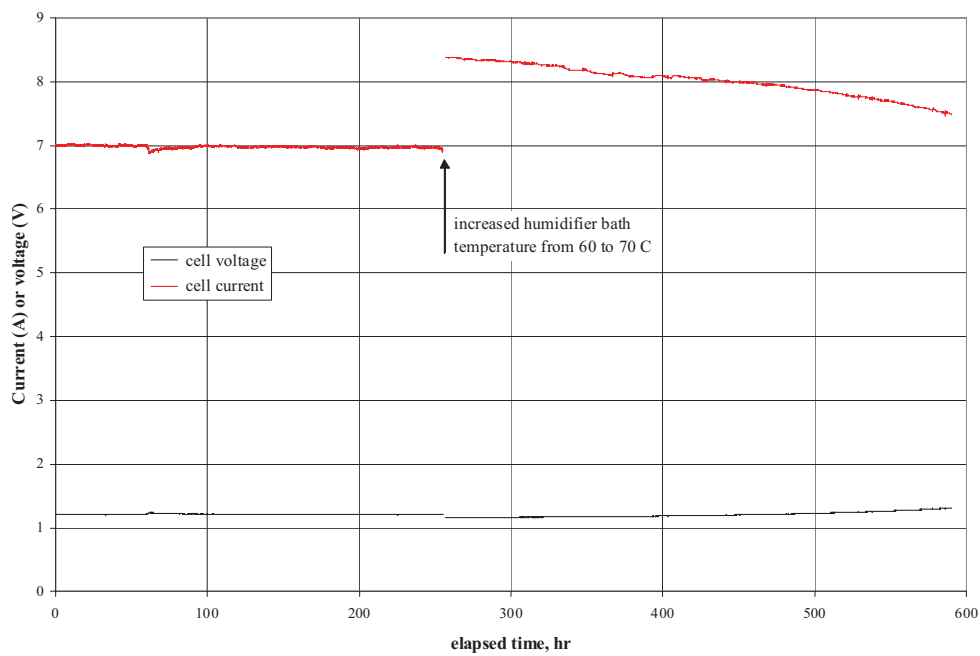


Figure 4-12. Cell voltage and current, long-term durability test.

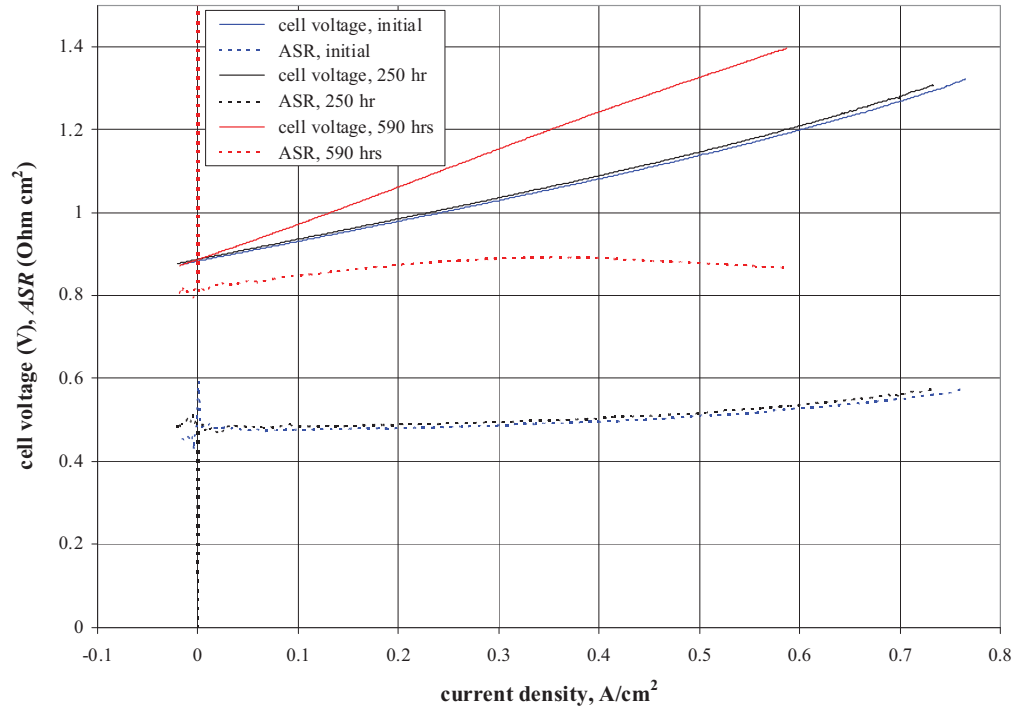


Figure 4-13. Cell voltage and ASR as a function of current density and cell operation time,  $T_{\text{dpi}} = 70^{\circ}\text{C}$ .

Cell voltage and current were very stable for the first 250 hrs of operation, indicating essentially zero performance degradation over that time period. However, after performing two sweeps at this time and increasing the bath temperature, performance degradation began to occur. This degradation is more evident in the plot of cell *ASR* presented in Figure 4-12. For the first 250 hours of operation, the cell *ASR* at the fixed operating condition of  $V_{\text{cell}} = 1.21 \text{ V}$  was nearly constant at  $\sim 0.67 \text{ Ohm cm}^2$ . After increasing the bath temperature, the *ASR* value immediately decreased to  $\sim 0.52 \text{ Ohm cm}^2$ , as discussed previously in conjunction with the sweeps. Thereafter, the *ASR* value begins to increase, attaining a value of  $0.90 \text{ Ohm cm}^2$  at 590 hrs. More durability testing with this type of cell will be required to determine the exact cause of the accelerated degradation that was observed with this cell after 250 hours. The most obvious culprit is the increased steam content, but the cell current also increased significantly and two sweeps were performed at 250 hours.

A final sweep was performed at 590 hrs. Figure 4-13 presents cell voltage and *ASR* values as a function of current density for three sweeps with the humidifier bath at  $70^{\circ}\text{C}$ . Cell voltage and *ASR* values for the initial sweep and the 250-hr sweep are nearly identical. However, for the 590-hr sweep, cell voltage increases much more rapidly with current density. In addition, the *ASR* values are much higher at 590 hrs. The plot of *ASR* versus current density at 590 hrs has a different shape than for the earlier times. This difference in shape is at least partially due to the fact that the cell voltage for this sweep exceeded the thermal neutral voltage of  $1.29 \text{ V}$ . Beyond the thermal neutral voltage, the cell begins to heat up, which results in a lower *ASR* value.

## 4.6 Post-Test Examination of Electrode-Supported Cells

The condition of each of the tested cells was examined upon removal from the test stand. The most obvious change in the cells after testing was associated with the reduction of the nickel oxide in the nickel-zirconia cermet steam/hydrogen electrode. This electrode forms the thick support substrate upon which the other thin cell layers (electrolyte and oxygen electrode) are deposited. The cell reduction procedure causes the color of the nickel cermet material to change from green to silver-gray. The cermet material otherwise appears to be very durable and does not show any evidence of damage or degradation after testing. A photograph of the nickel cermet of cell 316-03 after the 600-hour test is provided in Figure 4-14. It shows an impression of the nickel mesh on its surface, and the remnant of the alumina felt gasket around its outer edge, but is otherwise unremarkable. The air-electrode side of the same cell after the long-term test is presented in Figure 4-15. The air electrode shows the pattern of the array of square protuberances from the air flow distributor on its surface. It also shows localized delamination from the electrolyte. The cells that were tested for shorter time periods did not exhibit evidence of delamination. Delamination of the oxygen electrode has been identified as a possible degradation mechanism for solid-oxide electrolysis cells. It is more likely to occur in the electrolysis mode due to the direction of the oxygen transport. In the fuel cell mode, oxygen is removed from the air stream and diffuses through the porous cathode toward the triple-phase boundary at the electrode/electrolyte interface, driven by the concentration gradient created by the electrochemical reaction. In other words, in the fuel cell mode, there is an oxygen sink at the air-side triple-phase boundary. In the electrolysis mode, there is an oxygen source at the air-side triple-phase boundary such that oxygen is evolved from the electrode into the air-sweep gas stream. In this case, it is possible for the high pressures to develop within the oxygen electrode, especially if there is closed porosity. This pressure buildup can contribute to electrode delamination.

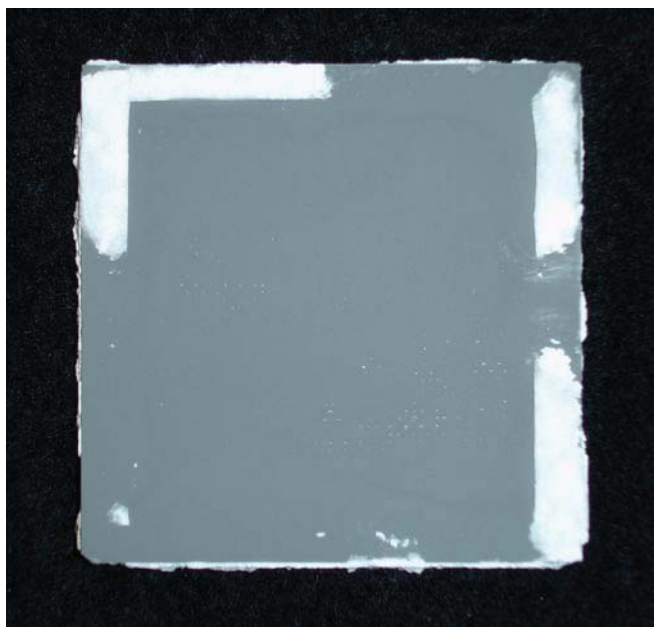


Figure 4-14. Closeup of steam/hydrogen electrode after 600-hour test, cell 316-09.



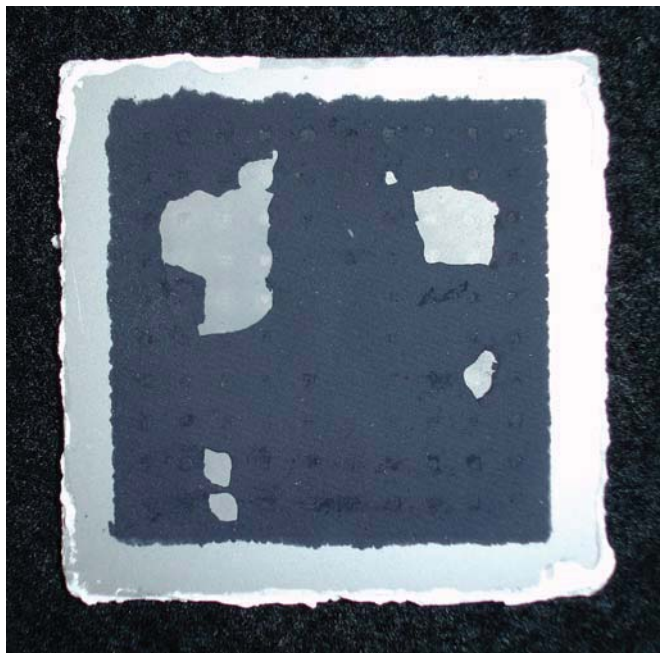


Figure 4-15. Closeup of oxygen electrode after 600-hour test, cell 316-09.

## 5. PERFORMANCE OF THE NASA BI-ELECTRODE SUPPORTED CELL

### 5.1 Button Cell Fabrication by NASA

The NASA cell is structurally symmetrical, with both electrodes supporting the thin electrolyte and containing micro-channels for gas diffusion, a bi-electrode supported cell or BSC. The electrodes are made by freeze-casting, a modified tape casting technique which creates the many micro-channels in the YSZ electrode green tape as shown in Figure 5-1. In freeze-tape casting an aqueous or organic slip is cast across a freezing bed and micron size ice crystals start to form at the Mylar side of the tape. The micro-crystals increase in size and form continuous ice crystals that grow larger towards the top, creating a natural gradient in porosity in the green tape; the green tape is placed in a freeze dryer and the ice crystals are removed by sublimation in a vacuum, leaving the micro-channels behind for gas flow. Symmetrical cells are fabricated by taking two green parts cut from the same piece of green freeze-cast tape, depositing a thin electrolyte layer between the tapes, and laminating the tapes together with the small pores facing each other, forming the YSZ tri-layer as shown in Figure 5-2. Cells, 2.54 cm O.D. (1") were prepared by firing the YSZ tri-layers at high temperature, followed by infiltration of the electrodes. Ni-nitrate was used for the SOFC anode and stoichiometric solutions of nitrates for the LSF cathode. Cells were allowed to dry/solidify prior to heat treatment for decomposition of the nitrates into metals or metal oxides depending on the electrode. This infiltration procedure was performed multiple times on both the anode and cathode to achieve suitable electrodes. The cells were then bonded to the end of a 1" O.D. YSZ tube using a high temperature glass ceramic (Figure 5-2).

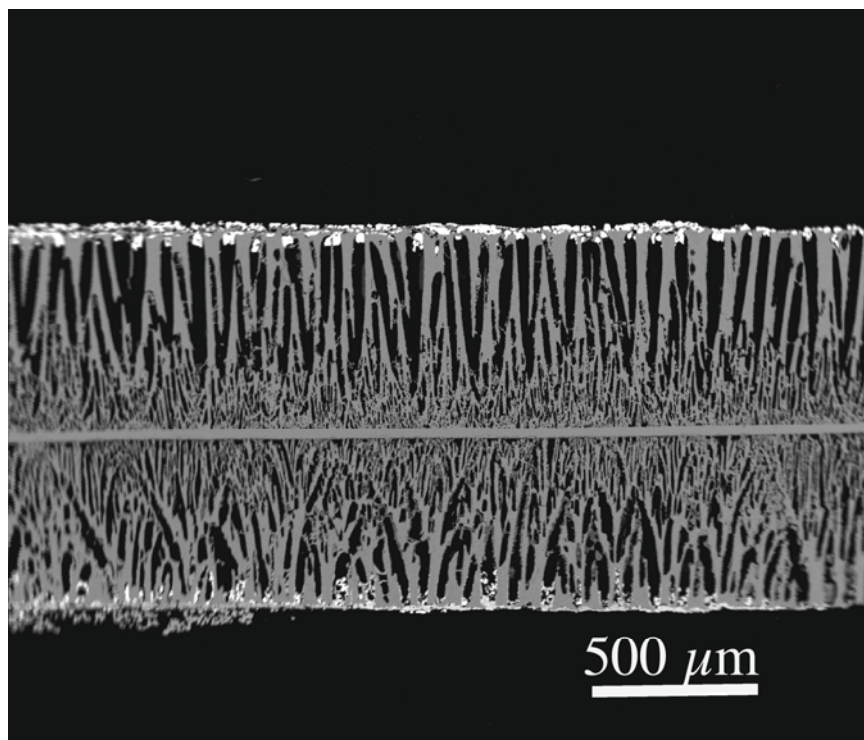


Figure 5-1. Cross section of a sintered BSC cell showing the thin YSZ (white) electrolyte in the center and the YSZ scaffolds, and the micro channels (black) formed by the ice crystals during freeze-casting, and then removed during freeze drying. The bright white at the top and bottom of the cell is Au ink.



Figure 5-2. NASA button cell mounted on support tube.

A Pt wire was placed on both sides of the cell to read the voltage and then Ni-mesh was used on the H<sub>2</sub> electrode and Ag mesh on the air electrode as current collectors; Au ink was used to attach the Pt wires for voltage measurement, and the other leads to the cells.

### SAMPLE BUTTON CELL TEST RESULTS

A total of 8 NASA button cells have been tested to date at the INL. Three cells were tested in October of 2008, four were tested in April of 2009, and 1 long duration test was conducted from July to September of 2009. Between the first two testing periods the testing apparatus was completely rebuilt and expanded, allowing simultaneous testing of two button cells and one stack. Tests #1-7 were conducted at a furnace temperature of 850 C, while test #8 was conducted at 800 C. Table 5-1. lists the various inlet conditions used for the cells. In the case of cell #7, testing was started with an inlet dew point of 50 C, but the inlet dew point was later increased to 62 C to avoid issues of steam starvation and improve cell performance.

Table 5-1. Cell test conditions.

Cell	H <sub>2</sub> Inlet (sccm)	N <sub>2</sub> Inlet (sccm)	Inlet Dew Point T (C)	H <sub>2</sub> O Inlet (sccm)	Inlet Mole Fraction H <sub>2</sub> O
1	63	350	50	70	0.14
2	60	230	77	282	0.49
3	60	300	60	110	0.23
4	50	350	50	68	0.15
5	50	350	50	70	0.15
6	50	350	50	68	0.15
7	50	350	50 / 62	68 / 138	0.17 / 0.35
8	50	205	79	294	0.54

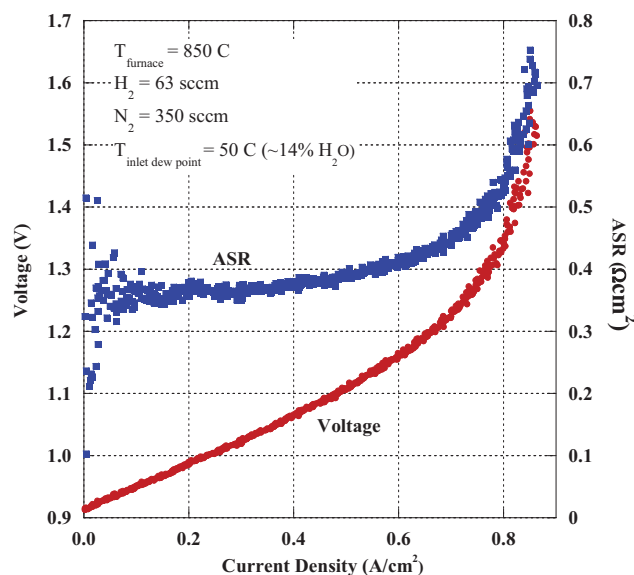


Figure 5-3. Polarization curve for first NASA cell tested.

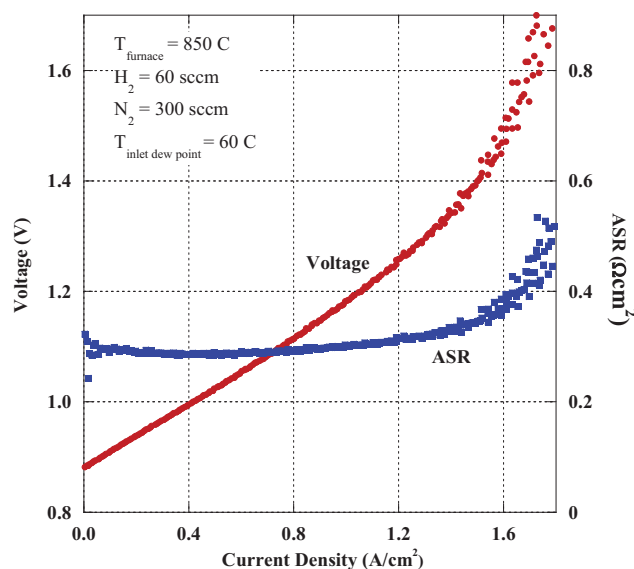


Figure 5-4. Polarization curve and respective ASR values for NASA cell 3.

Figure 5-3 and Figure 5-4 represent results of a voltage sweep / polarization curve test for NASA cell 1. The VI curve and resulting area-specific-resistance (ASR) curve are shown in Figure 5-3. The VI curve is relatively linear for current densities less than  $0.6 \text{ A/cm}^2$ . The non-linearity of the VI curve (and ASR curve) for higher current densities is indicative of steam starvation. At a current density of  $0.6 \text{ A/cm}^2$ , the steam utilization was only approximately 20%. Starvation was not due to high steam utilization but due to the relatively low inlet steam flow rate. Scatter in the ASR values at low current densities is due to difficulties in measuring extremely low current values.

Figure 5-5 presents the inlet / outlet gas mixture dew point values as well as hydrogen production rates. Two different calculated hydrogen production rates are shown: hydrogen production estimated rate from the difference between outlet and inlet dew points, and hydrogen production rate estimated from the cell current

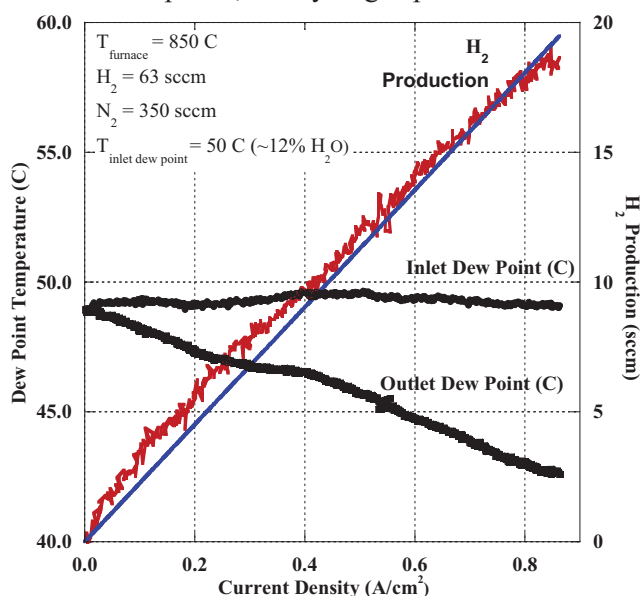


Figure 5-5. Dew points and  $\text{H}_2$  production rates for polarization curve in Figure 5-3.

(Faraday's Law). As the cell voltage and current increase, steam is consumed. The measured outlet dew point drops in value while the measurement of hydrogen production rate increases in value. The good agreement between the two independent measurements of hydrogen production rate indicates negligible cell leak age and no cell electrical shorting.

Figure 5-6 and Figure 5-7 show voltage sweep / polarization curve test results for NASA cell 3. This test used a higher inlet steam flow rate and thus could sustain a significantly higher current density before becoming steam starved. For this cell and these test conditions, starvation was not noted until current densities in excess of 1.4 A/cm<sup>2</sup>, or steam utilizations of 30% and greater. ASR values for this cell were roughly the same as for cell 1.

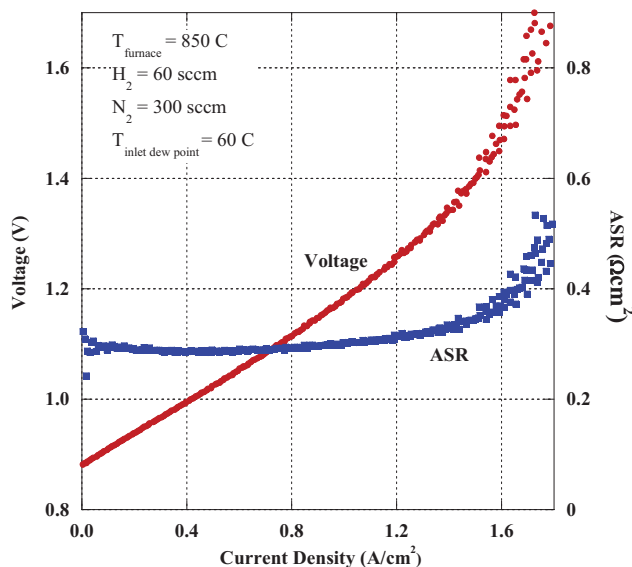


Figure 5-6. Polarization curve and respective ASR values for NASA cell 3.

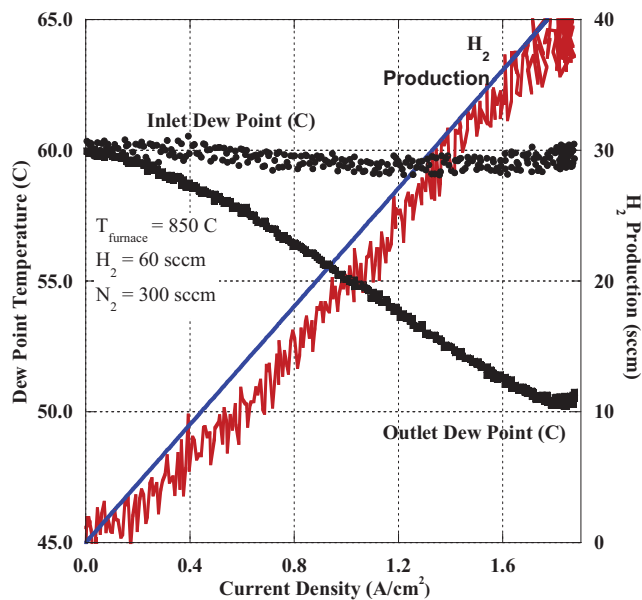


Figure 5-7. Dew points and H<sub>2</sub> production rates for polarization curve in Figure 5-5.

Test results for cell 5 are found in Figure 5-8. This cell was tested in the newly refurbished testing apparatus. In this case, the voltage sweep extended slightly into the fuel cell range of operation. The lower limit for the voltage sweep was determined by the ability of the power supply to sink the current produced by the cell. The resulting polarization curve remained linear through zero current density, indicating low activation polarization. The average ASR for the sweep was  $0.33 \Omega\text{cm}^2$ .

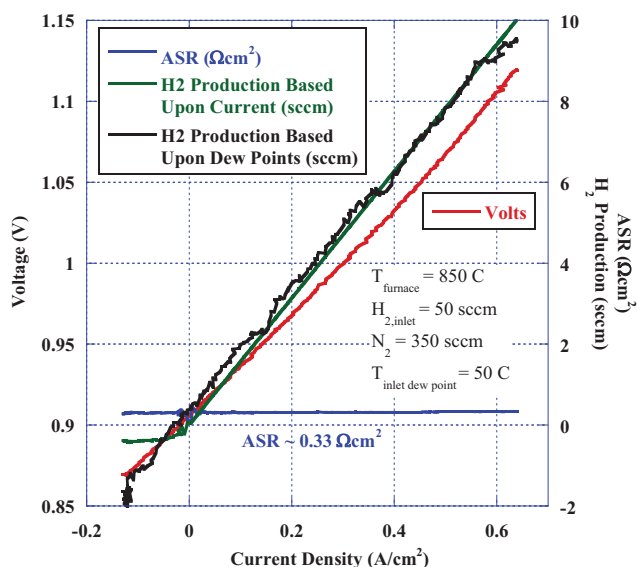


Figure 5-8. Polarization curve and  $\text{H}_2$  production rates for NASA cell 5.

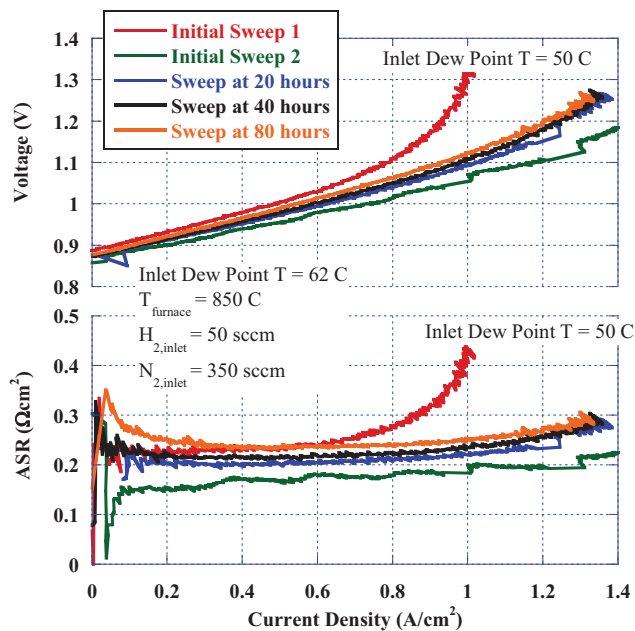


Figure 5-9. Summary of polarization curves for NASA cell 7



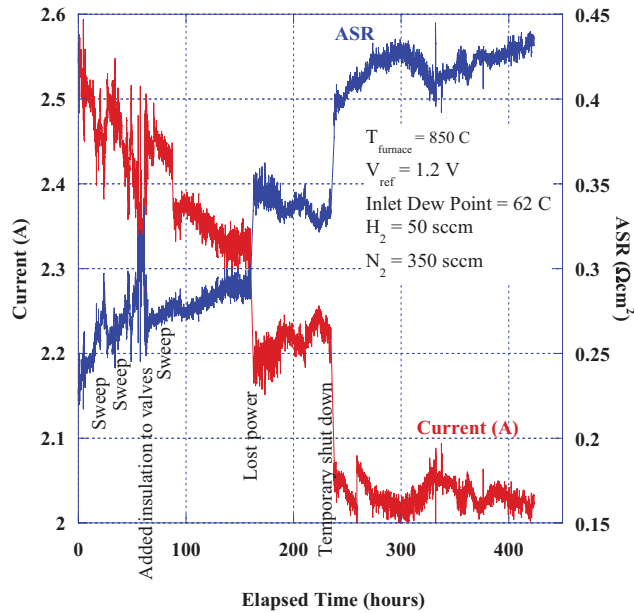


Figure 5-10. Long duration test data for NASA cell 7.

NASA cell 7 was the most extensively characterized of the cells tested to date. Two initial voltage sweeps / polarization curve tests were performed, after which the cell was allowed to run in a steady state, long duration mode for over 420 hours. During this extended period of operation, three additional voltage sweeps were performed: at 20 hours, 40 hours, and 80 hours elapsed test time. Figure 5-9 summarizes the voltage sweeps. The first sweep was run for an inlet dew point of 50°C, whereas the inlet dew point temperature for the remaining sweeps was 62°C. Steam starvation was only observed in the first (low inlet dew point temperature) sweep. Comparison of the four subsequent voltage sweep shows that the ASR values gradually deteriorated with time, indicating a slow degradation in cell performance.

Figure 5-10 presents the long duration test data for NASA cell 7. After initial characterization, the cell voltage was set to 1.2 volts. The test was continued for 420 hours. Three voltage sweeps / polarization curves were generated during long duration testing, as indicated on the figure. Three other perturbations occurred during long duration testing. At 64 hours long-term test duration additional heat trace heaters and insulation were added around some valves in the test apparatus. This was done to prevent the formation of condensation, and seemed to temporarily improve the cell ASR. At 160 hours elapsed test time there was a loss of facility power. Since the computer for the data acquisition system was not powered via an uninterruptible power supply, there was a loss of control and the cell furnace cooled about 150 C to 700 C. This disruption caused the cell ASR to climb from 0.28  $\Omega\text{cm}^2$  to 0.34  $\Omega\text{cm}^2$ . The cell did recover somewhat, but at 235 hours test duration the computer lost communication with the data acquisition system due to a faulty cable. This again required several hours to repair, during which time the furnace cooled to 550 C. During this period, the cell ASR deteriorated from 0.33  $\Omega\text{cm}^2$  to 0.4  $\Omega\text{cm}^2$ . The loss of power and the loss of communications were the dominant contributors to degradation in the cell's performance.

NASA cell 8 was heated to an operating temperature of 800 C rather than 850 C, and with higher inlet steam content than previous cells. A voltage sweep was initiated from 0.8 V to the thermal neutral voltage. The sweep data is shown in Figure 5-11. The sweep average ASR was approximately 0.21  $\Omega\text{cm}^2$ . Current densities approached 2.5 A/cm<sup>2</sup> at the thermal neutral voltage. Actual cell amperages approached 5 A. This high cell current load caused the current-carrying cell leads to fail. Rather than cooling down the cell and repairing the broken leads, it was decided to use the reference voltage leads as current-carrying leads for the remainder of testing. These leads were significantly smaller in cross section and necessitated limiting the cell current to a much lower value of about 0.38 A (0.19 A/cm<sup>2</sup>).

Figure 5-12 summarizes the long duration test data for NASA cell #8. Unfortunately, the first 340 hours of test data were not recorded. From 341 hours test duration to 888 hours test duration, the cell ASR increased from  $0.68 \Omega\text{cm}^2$  to  $0.80 \Omega\text{cm}^2$ , which corresponds to a degradation rate of 32%/1000 hrs.

To summarize INL testing of NASA bi-supported cells: overall the cells performed well, especially considering that these are first generation cell designs. They were designed for high power-to-weight performance, which is evident in their low initial ASRs and high current densities. Initial performance, as measured by ASR values, was good. Two relatively long duration tests were conducted which showed quite high degradation rates.

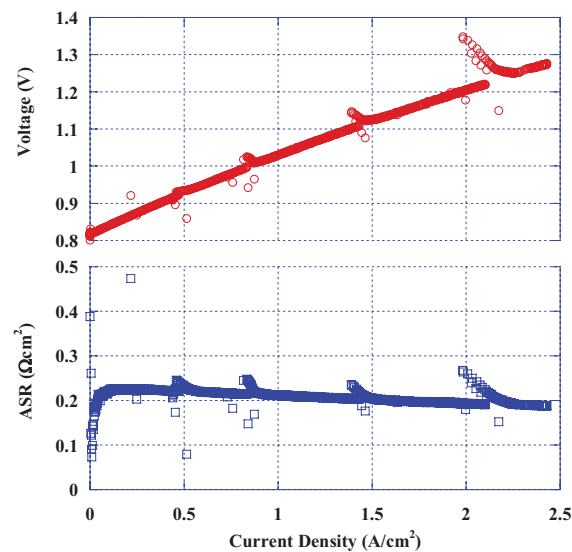


Figure 5-11. Polarization curves for NASA cell 8.

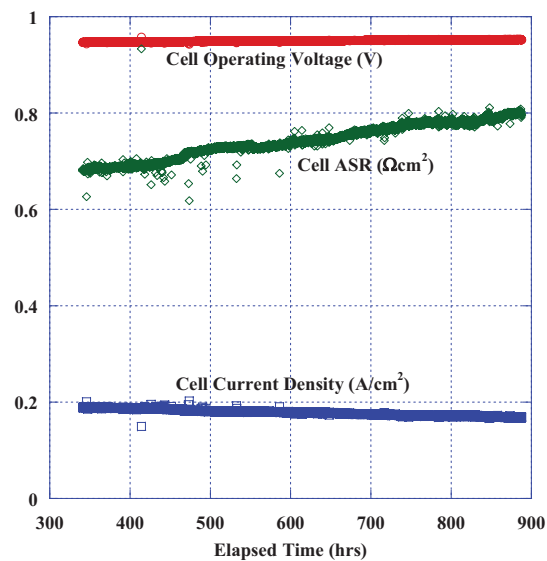


Figure 5-12. Long duration test data for NASA cell 8.



## 6. IMPROVED CERAMATEC CELLS

### 6.1 Cells Tested at INL

The INL ILS cells / stacks were manufactured by Ceramtec Inc. Figure 6-1 shows the Ceramtec stack construction. These consisted of a Sc-stabilized zirconia electrolyte (approximately 200  $\mu\text{m}$  thick), nickel cermet hydrogen electrode, and manganite oxygen electrode with a cobaltite current distribution layer. Interconnect separator plates were stainless 400 with rare-earth scale treatment and a cobaltite current distribution layer on the air side. The air side flow channel was a corrugated foil of Hastalloy with scale treatment and a fired cobaltite layer. Stainless 400 edge rails were treated with a ceramic coating to inhibit corrosion. The hydrogen-side flow channel was an untreated Ni201 corrugation.

Post-test evaluation of the cells by the cell manufacturer Ceramtec indicated:

- Hydrogen electrode appeared to be in good condition
- Oxygen electrode showed some delamination with an apparent foreign layer deposited at the electrolyte interface.

These cells were also examined by Argonne National Laboratory and the Massachusetts Institute of Technology. Their analysis showed that the  $\text{O}_2$ -electrode delaminated from the electrolyte near the edge. One possible reason for this delamination is excessive pressure buildup due to high  $\text{O}_2$  flow in the over-sintered region. Furthermore, electrochemical reactions were also identified as a cause of degradation. Two important degradation mechanisms were examined: (1) transport of Cr-containing species from steel interconnects into the oxygen electrode and cobaltite bond layers in SOECs, and (2) cation segregation and phase separation in the bond layer.

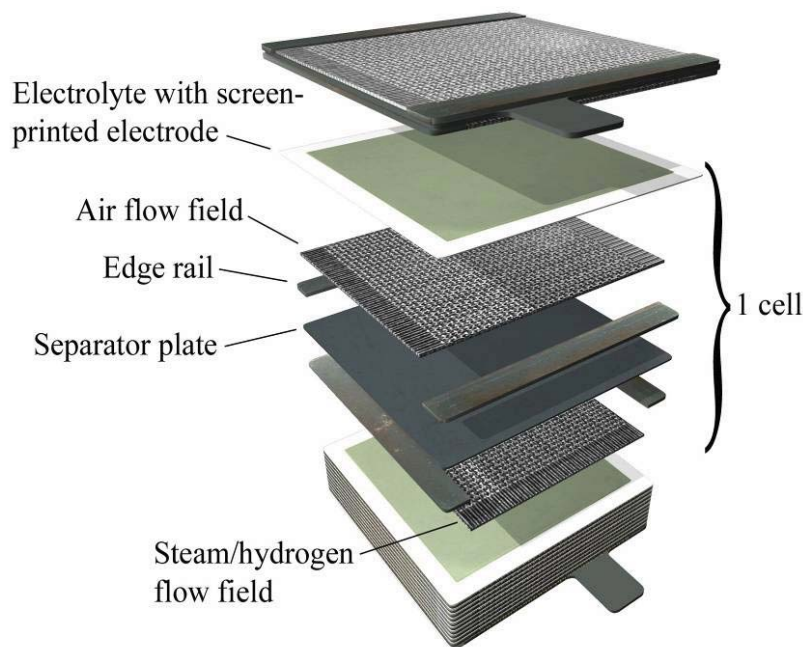


Figure 6-1. Ceramtec stack configuration.

These post-test examinations prompted Ceramtec to develop a new oxygen-side electrode composition. Second in priority, Ceramtec also began development of a fully-stabilized Sc-zirconia electrolyte material. The new oxygen-side electrode was first tested at the INL as a 10-cell stack to fulfill a 2500 hour long-duration test milestone. The fully-stabilized electrolyte concept was first tested at the INL as a button cell.

On July 25, 2009, long duration testing began of a fully-stabilized electrolyte button cell from Ceramtec. This cell had the traditional oxygen-side electrode, rather than the more advanced electrode material used in the 2500 hour test. Figure 6-2 is a complete test history to date for this button cell. At 64 hours elapsed test time, the electrolysis power supply was switched from constant output to feedback control based upon the cell operating voltage. At this time, the cell operating voltage was set to thermal neutral (1.29 V). The cell degraded quite quickly, as can be seen from the ASR curve in Figure 6-2. This seems to indicate that the primary explanation for cell degradation in electrolysis mode of operation involves the oxygen-side electrode. Future plans call for testing another advanced cell made up of a fully stabilized electrolyte with the advanced oxygen-side electrode material.

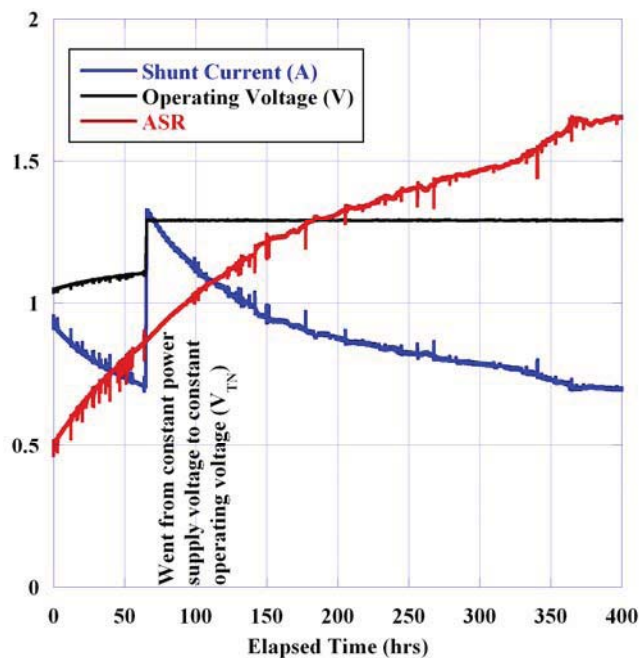


Figure 6-2. Performance of the Ceramtec fully-stabilized electrolyte button cell.

## 6.2 Stack fabrication and testing summary for stack tests performed at Ceramatec.

Eight stacks were built and tested to evaluate and understand how certain material changes can affect the long term stability in a HTE stack. Most changes were evaluated first with sample coupons and/or button cells, and then tried in stacks after improvement was shown. Some of these tests were performed under a Ceramatec project funded by the Office of Naval Research and are included to show progression of work leading to improvement in performance stability of electrolysis stacks.

Modifications were also made to the test stand. These included a ceramic coating of the gas inlet piping, a ceramic plasma coating the sweep air plenum, using an oil free vane pump in place of compressed air, and replacing the brass spargers with stainless steel in the bubblers. These modifications were evaluated to determine if stack performance degradation was related to the test stands. The vane pump and coated air plenum may not provide any benefit, but more testing will be needed to see if the tube coating is needed.

Stack 493 was built with standard cells like those in the ILS test, but the air side of the interconnect plates and the flow fields did not have any cobaltite coating. This was a 5-cell stack that was tested to see if removing the cobaltite from the metal parts would hinder chromate formation. This stack had very low current (1.15 amps) when it was placed under load for the long-term test. The stack was cooled down after 168 hrs of operation and had a degradation rate of 155%/1000 hrs. The conclusion was that the interconnects need to have a current distribution layer to achieve lower ASR values.

Stack 494 was built with left-over components from the ILS test to evaluate the effect of the test stand modifications. This stack was tested in fuel-cell mode and it showed evidence of fuel starvation during the sweep. When the bubbler was heated and the stack was under long-term load, the water level in the bubbler was very erratic and pulsed due to back pressure. This stack ran 140 hrs with a degradation rate of 130%/1000 hrs. When the stack was dismantled, about 50% of the fuel channels in the top cells were blocked by seal paste, which is the reason that cell was working poorly. The fuel inlet line was removed and blown out with compressed air and large particles of the ceramic coating were removed, which was the reason the bubbler was pulsing. This ceramic coating was applied to the inside of the reactant feed lines to suppress Cr vapor transport. It is very difficult to apply an adherent ceramic coating to the inside of a small tube.

Stack 495 was built to evaluate the effect of coating the interconnects and air-side flow fields with spinel, and to evaluate the new cobalt ferrite oxygen electrode. All interconnects were the same but half of the cells in the stack used the standard manganite with cobaltite oxygen electrodes and the other half used the cobalt ferrite electrode and bond layer. The initial ASR was 2.19 for the standard cells and 2.34 for the new oxygen electrode cells. After the first 200 hrs the stack was operating at a lower ASR than when it started and the stack was heated to 830°C to try and increase the degradation rate. The segments that had the standard cells degraded while the segments with the new electrode improved or stayed steady. This test demonstrated that the spinel interconnect coating gave a significant reduction in stack degradation, but also resulted in a reduction in initial performance. It also showed that the new electrode was more stable than the standard oxygen electrode.

Stack 496 was a repeat of the better segment from stack 495. This stack had the spinel coated interconnects and air side flow fields as well as having the new cobalt ferrite oxygen electrode. This stack had an initial ASR of 2.46 in HTE at 800 C with an 83°C bubbler. Several operational parameters were evaluated to improve the ASR during the long term test. Some of these are

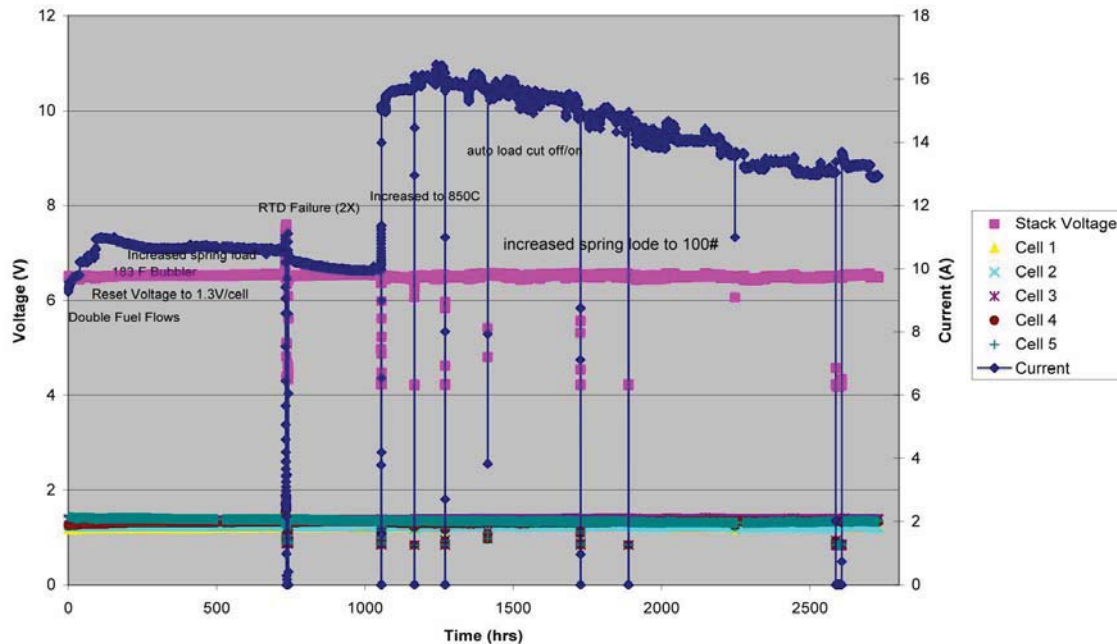


Figure 6-3. Long-term performance (>2500 hrs.), stack 496, tested at Ceramatec.

noted on the long-term plot, Figure 6-3. This stack has also gone through a few minor thermal cycles, bubbler cool offs, and auto load interruptions, which have caused some step changes downward in performance. This stack is still in operation and the degradation rate appears to be slowing down.

Stack 497 was built like stack 496 and installed at INL for the 2500 hr milestone test.

Stack 498 was a 5-cell stack of similar construction to stacks 496 and 497 but had a green nickel cermet bond layer on the fuel side instead of the green Ni layer and it had a fired layer and green layer of cobalt ferrite on the air side electrode. These changes were based on button cell tests that showed good stability. The stack had high ASR initially (over 6), but it continually improved for the first 150 hrs when it was placed in fuel-cell mode over night to see if that would help performance. The stack was placed back in HTE mode and was operated in HTE mode for a few days at about 8 A (increase from before). The stack was heated to 900 C to densify the green layers and it operated at 26 A for about a day then started to degrade and was cooled back down to 800 C where it returned to about 9A, but with a higher degradation rate than before. The conclusion from this test was that the nickel cermet needs to be fired before testing and that 900°C operation does increase the degradation rate.

Stack 499 was built to evaluate the performance of the new electrode with the old cobaltite coated interconnects. Initial HTE ASR was 1.65 which is an improvement over the spinel coated icons. This stack was placed under long-term load, initially at 14.8 A, with increased performance for the first 20 hrs to over 17 A. It then began to degrade until it was cooled off at 480 hrs with a load of 11.8A. The degradation rate was 41%/1000 hrs which is an improvement over the manganite electrode with the same type of interconnects (130% in stack 494), but still quite high.

Stack 500 was built with the spinel-coated interconnects and air side flow fields and the new cobalt ferrite composite electrode, but on the fully stabilized Sc electrolyte. The initial performance was better at 1.72 ASR and it has been running for over 800 hrs at 800 C with fairly linear degradation of 25%/1000 hrs. This performance was not as good as what we had observed with stack 496.

Stack 501 was built like stack 496 but the air-side flow fields were spray-coated with a conductive ink. This coating was intended to improve the electrical contact and current-carrying ability of the flow fields as had been shown in half-cell coupon tests. Initially this stack had an ASR of 1.36 at 800C in HTE mode. This is near what we would get with the old standard stack components. However, the degradation is higher than stacks 496 and 500 at about 66%/1000 hrs. This degradation is still better than the old cobaltite coating with the manganite electrode, but not good enough. This does show us that we need to find a better conductor for the interconnects and flow fields if we are going to use the cobalt ferrite electrode and spinel coated Icons.

### **6.3 Button cell fabrication and testing summary for tests performed at Ceramatec.**

In order to characterize the baseline cells, cell performance and degradation were evaluated by V-I sweep in fuel cell and electrolysis modes. In order to mitigate cell degradation, cells with a new electrolyte (fully stabilized Sc doped), electrode materials (cobalt ferrite oxygen electrode and cobaltite bond) were also characterized for long-term tests.

The electrolytes were fabricated by tape casting and sintering process. The nickel cermet hydrogen electrode was screen-printed and sintered. Then the oxygen electrode was screen-printed on the other side of the electrolyte and fired. Finally the bond layers were screen printed on the fired electrodes. The baseline cells were fabricated using the same batch of nickel cermet, Ni bond, manganite electrode and cobaltite as bond layer.

Cells were characterized by V-I sweep in SOFC and SOEC modes. The area specific resistance (ASR) extrapolated from the slope of V-I polarization curve was used as the criteria for cell performance. Most of the baseline cells were tested in glass seal rig. Several cells were tested using a specially designed pressure fixture. Each cell was secured at the end of an alumina tube with the hydrogen electrode facing the inside the tube. Mica gasket was used as a seal. The cell was held by spring load and the rig was put in the hot zone of the furnace. The hydrogen electrode was reduced in H<sub>2</sub> overnight. Voltage vs. current density polarization curve was measured on the cell. Long term testing in the electrolysis mode was performed on several cells for stability characterization.

Baseline Cells Test: Six baseline cells were tested in both SOFC and SOEC modes as shown in Figure 6-4 to Figure 6-9 (Bline252 to Bline263). The cell ASR for fuel cell mode ranged from 0.774 to 0.835. Two cells were tested in pressure as shown in Figure 6-4 and Figure 6-9 for Bline252 and Bline 263 respectively. The high OCV shows the new glass-free seal is satisfactory for SOFC test. For electrolysis mode the cell ASR varies from 0.694 to 0.796. This batch of baseline cells shows consistent performance. Note that the OCV in electrolysis mode is around 0.92, which suggests no condensation occurred along the gas line. Also no concentration polarization was observed for SOEC mode.

Cells with Cobalt Ferrite oxygen electrode: Figure 6-10 and Figure 6-11 show the V-I curves for cells with cobalt ferrite electrodes. Cell 266 had a cobalt ferrite bond layer and shows better performance than cell 260 which had a cobaltite bond layer, which needs to be characterized further if the bond layer caused the performance difference.

Fully vs partially stabilized electrolyte: Figure 6-10 shows the performance of cells with fully stabilized electrolyte, which didn't show higher performance than that with partially stabilized electrolyte, even though the conductivity measurements shows the fully stabilized material has two times the conductivity of the partially stabilized material. Also the fully stabilized electrolyte is mechanically weaker as



compared to partially stabilized electrolyte, and more likely to cause catastrophic cracking if used in stacks.

Manganite vs. Cobalt Ferrite oxygen electrode: The only difference between Cell 266 and baseline cells is the oxygen electrode and bond layer materials. It is interesting to compare the performance of Bline252 and Cell 266. Both cells were tested in the pressure rig and with  $1.5 \text{ cm}^2$  electrode area. Cell 266 shows higher performance in both SOFC and SOEC modes, although materials with much lower conductivity were used, which means the conductivity of materials is not the only criterion to decide which material is good as electrode. It is surmised that the bond layer works not only as an electronic conductor but also as an ionic conductor.

Nickel cermet bond layer vs. Ni bond layer: Cell Bline252 and Cell 266 are shown in Figure 6-4 and Figure 6-11 and were tested in the pressure rig. These two cells show higher ASR for electrolysis mode than that in fuel cell mode. In contrast, Cell 260 with nickel cermet bond layer as shown in Figure 6-10, exhibits a similar ASR for fuel cell mode and electrolysis mode. A higher ASR for electrolysis mode in the pressure rig and glass-free seal has been frequently observed. The higher ASR may be the result of the oxidation of Ni bond from the leakage of glass-free seal. It is suggested that for large cells, the redox-tolerant nickel cermet bond layer can be used to decrease ASR in electrolysis mode in which a glass-free seal is used.

Fully stabilized Sc doped electrolyte: A cell with fully stabilized electrolyte (Cell 309) shows higher performance than one with partially stabilized electrolyte and it has a slightly lower OCV. SOFC (ASR: 0.863), SOEC(ASR:0.918).

Long Term Test in Electrolysis Mode: Long term tests (Figure 6-12 through Figure 6-17) in SOEC mode were carried out on baseline cells and cells with cobalt ferrite oxygen electrode. Four of five baseline cells exhibited 50% degradation in 200 hours. One of them shows 32% degradation. The cells with the cobalt ferrite oxygen electrode show 35% degradation. SEM and EDS need to be performed to see the microstructure of electrode and electrode for the tested cells.

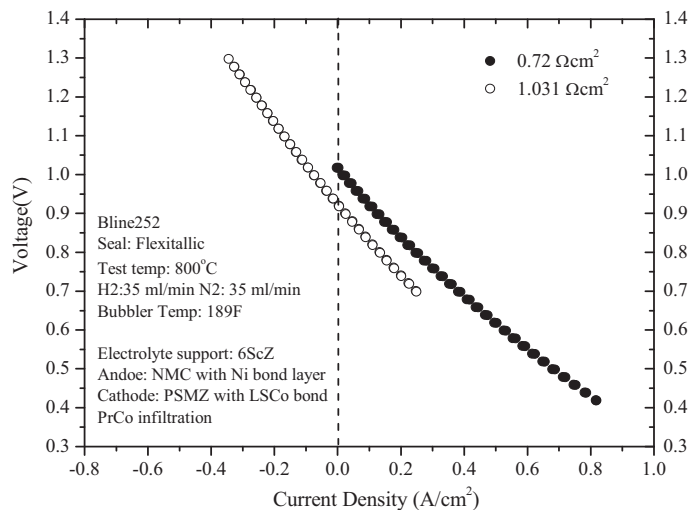


Figure 6-4. Baseline polarization curves, cell 252.

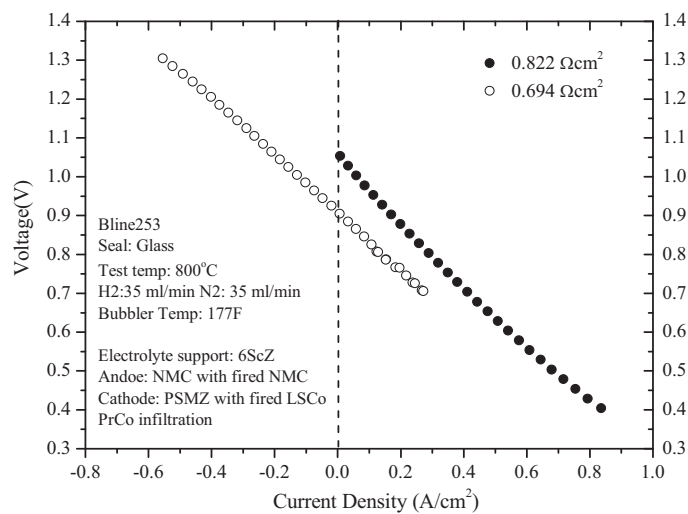


Figure 6-5 Baseline polarization curves, cell 253.

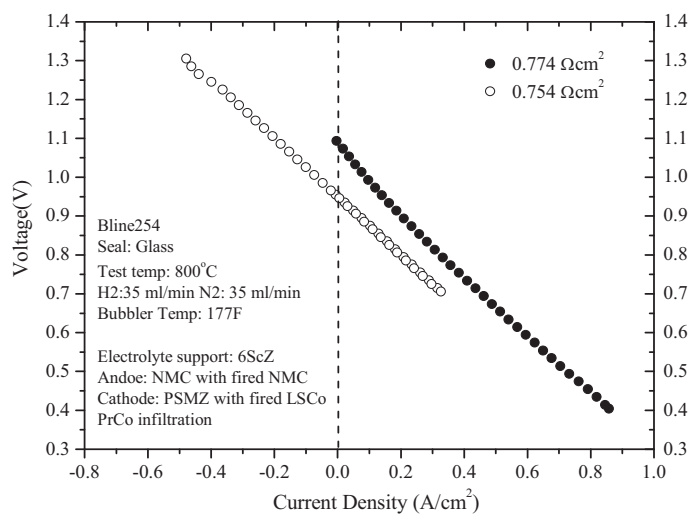


Figure 6-6. Baseline polarization curves, cell 254.

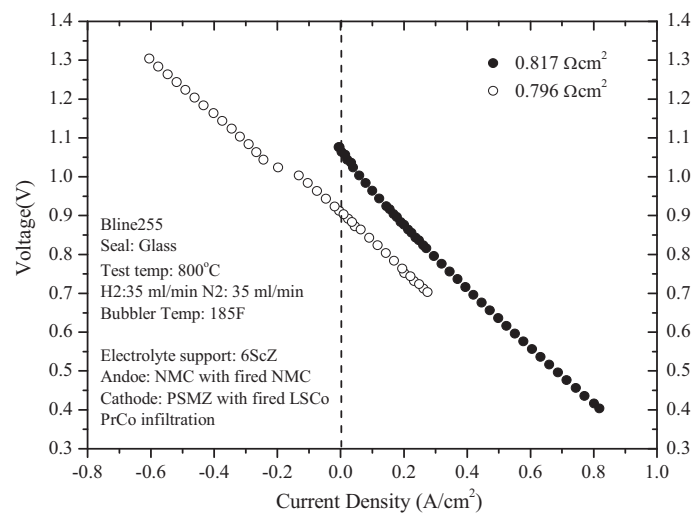


Figure 6-7. Baseline polarization curves, cell 255.

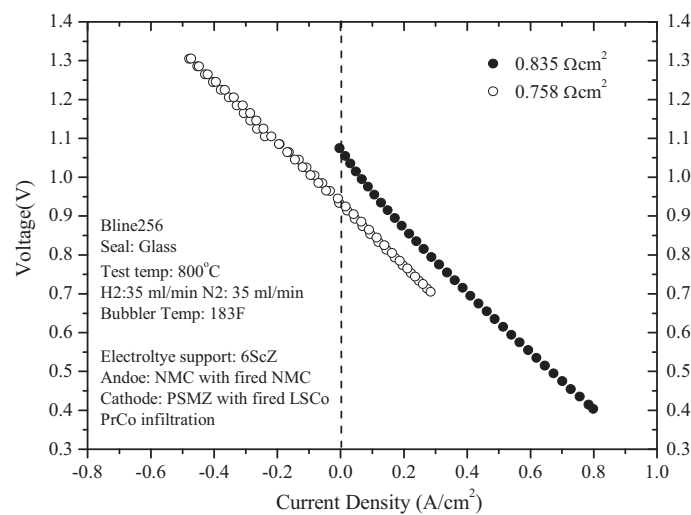


Figure 6-8. Baseline polarization curves, cell 256.



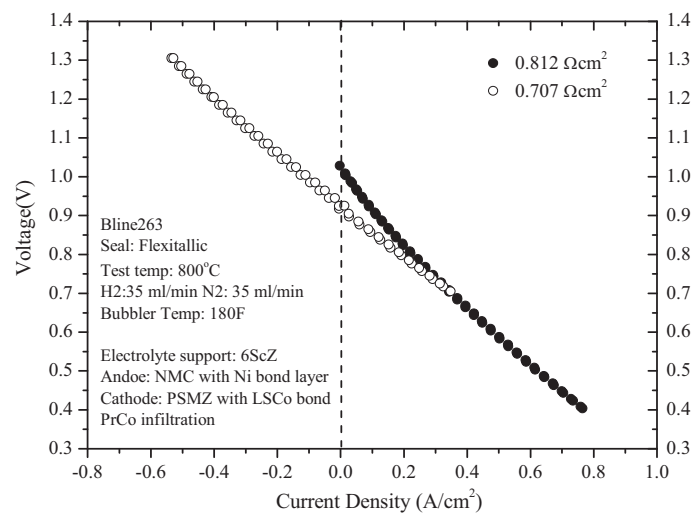


Figure 6-9. Baseline polarization curves, cell 263.

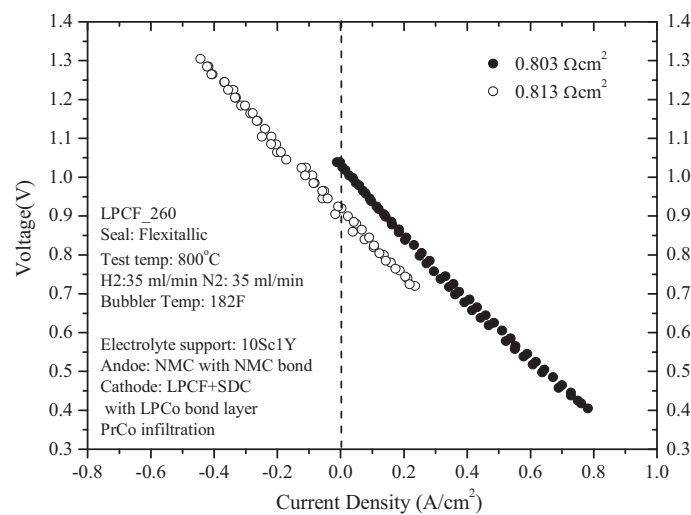


Figure 6-10. Polarization curves, LPCF cathode, cell 260.

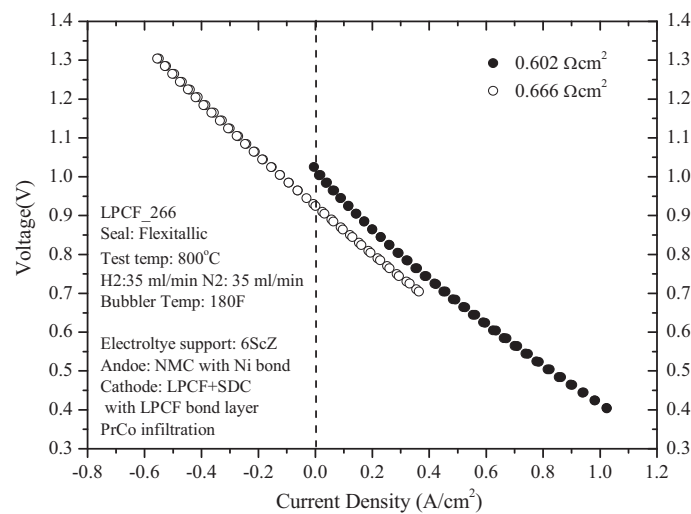


Figure 6-11. Polarization curves, LPCF cathode, cell 266.

### Long term tests

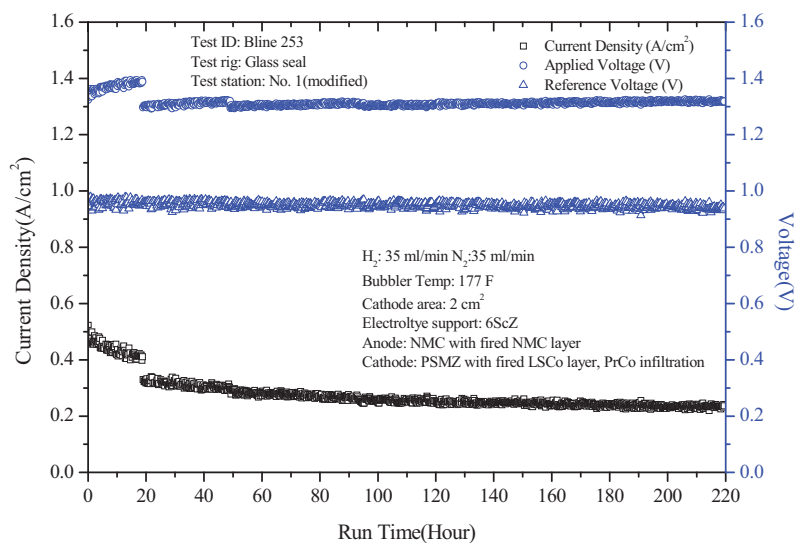


Figure 6-12. Long-term test, baseline cell 253.

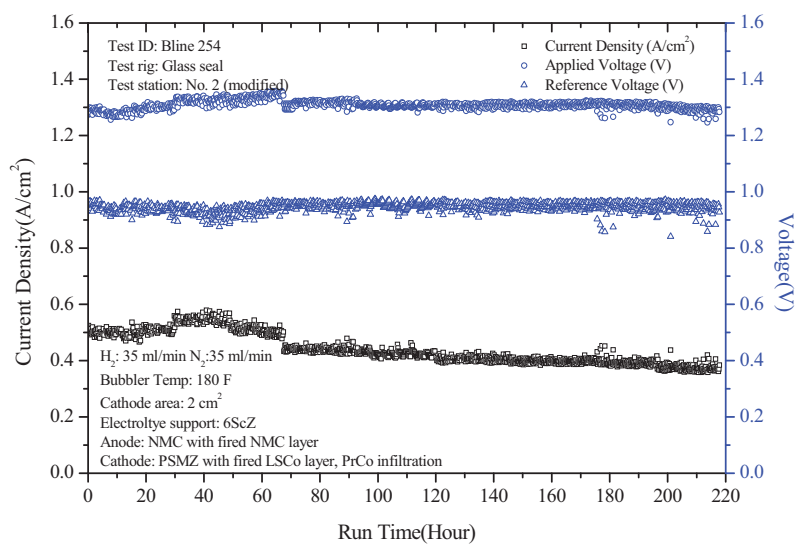


Figure 6-13 Long-term test, baseline cell 254.

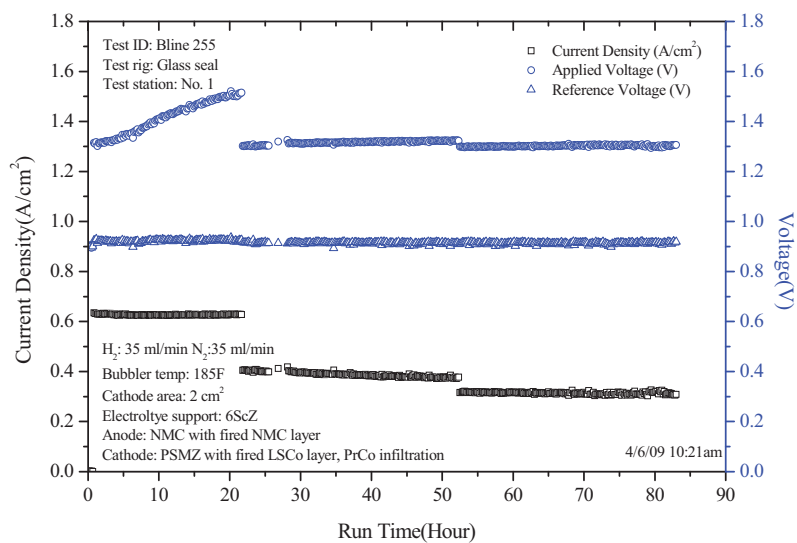


Figure 6-14 Long-term test, baseline cell 255.

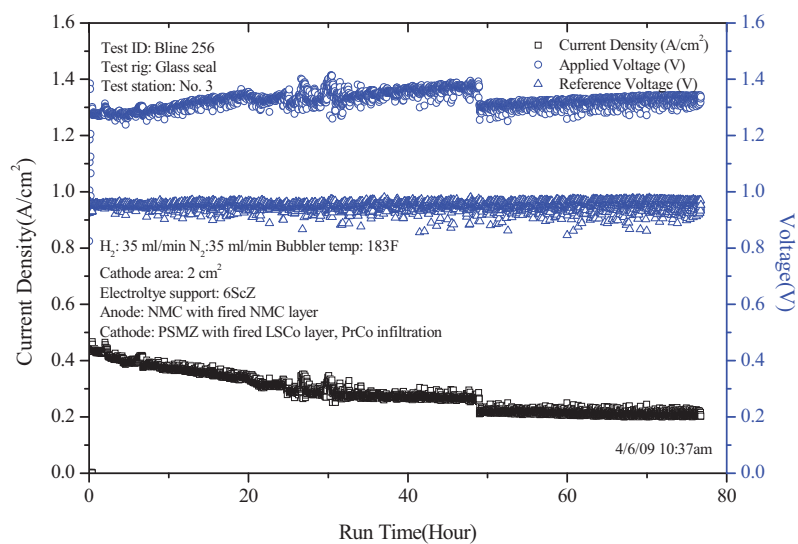


Figure 6-15 Long-term test, baseline cell 256.

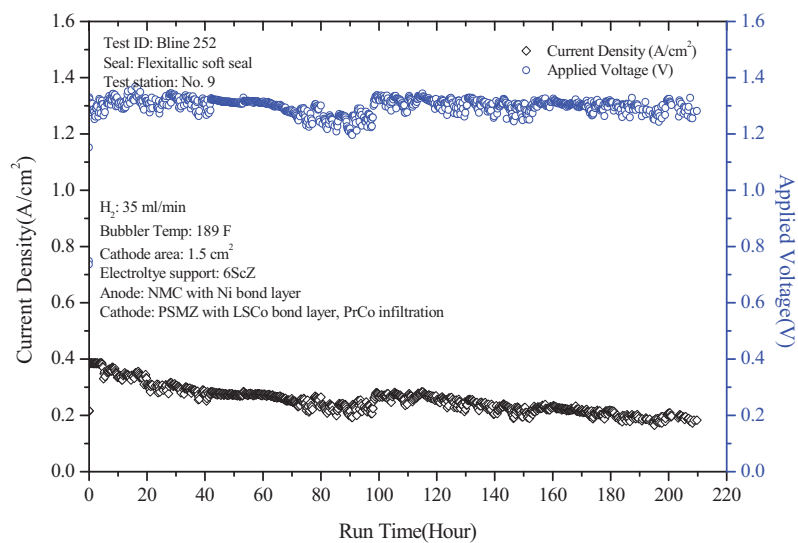


Figure 6-16 Long-term test, baseline cell 252.

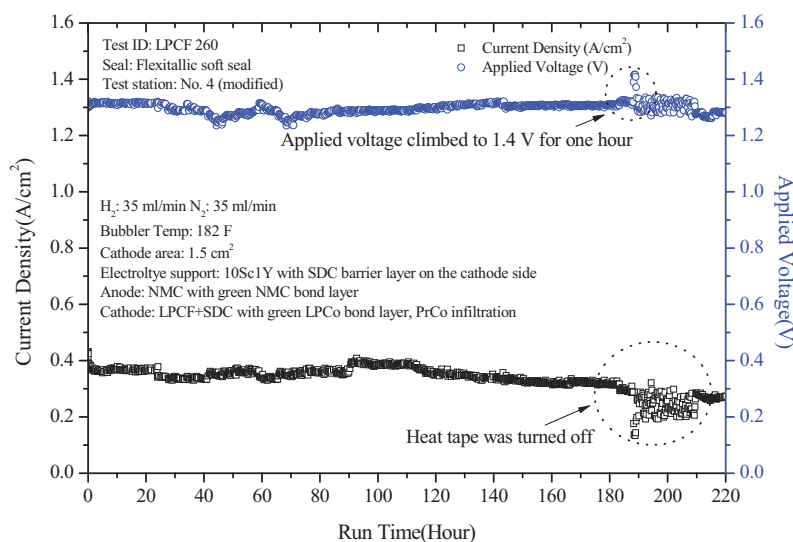


Figure 6-17 Long-term test, LPCF cathode, cell 260.

## 6.4 Summary and Future Work - Ceramatec

Baseline cells show consistent performance in both SOFC and SOEC modes. Long term tests on baseline cells suggested more work may need to be done to improve the stability of the baseline cells. 10Sc1Y electrolyte may not be a good option as electrolyte materials. Cell with LPCF electrode shows better performance than that of PSMZ. NMC bond layer may be used with glass-free seal to resist redox. Also cell with 10/6 ScZ blend electrolyte shows stable long-term performance.

## **7. DEGRADATION STUDIES OF ELECTRODE-SUPPORTED SOLID-OXIDE ELECTROLYSIS CELLS IN A 5-CELL STACK CONFIGURATION AT MSRI**

### **7.1 Background:**

Battelle Energy Alliance, LLC (BEA)/Idaho National Laboratory (INL) is continuing a research and development project to develop a high temperature steam electrolysis system for hydrogen production. The electrolysis system utilizes high-temperature process heat and electrical power to split hydrogen from steam using solid oxide electrolysis cells (SOECs). A key factor in developing a robust SOEC technology is to understand the degradation mechanisms and to develop viable strategies to mitigate degradation. MSRI has studied several possible chemical and structural degradation mechanisms in SOECs and provided information aimed at reducing degradation in future SOECs. The objective of the project was to develop a promising, degradation-resistant SOEC technology consisting of the MSRI's proprietary material compositions that had demonstrated high stability in laboratory tests.

### **7.2 Status:**

#### **Task 1 – Fabrication of Planar, Electrode-supported Cells and Related Stack Components for SOECs**

MSRI has successfully fabricated planar, Ni+YSZ-based negative electrode-supported SOECs following MSRI's standard cell fabrication procedure to ensure cell quality. Starting from the as-received powders, NiO and YSZ were mixed with binders and solvents and ball-milled to form slurry, followed by casting over a precision surface with a doctor blade dispensing the slurry. After drying in air, green tapes with a desired thickness were formed. The green tapes were then laser cut followed by bisque firing. Graded negative electrode functional layers and the electrolyte layer were applied by spray-coating. The multi layer structure was sintered in air at elevated temperatures. A (La, Sr)MnO<sub>3</sub>-based positive electrode functional layer and a current collecting layer were screen-printed, followed by firing in air at elevated temperatures. Typically, a completed cell had five distinct layers: a Ni+YSZ-supporting substrate, a Ni+YSZ negative electrode interlayer, a thin film electrolyte, a composite positive electrode interlayer, and a positive electrode current collecting layer with 100 cm<sup>2</sup> active area.

Three sets of SOECs with different material compositions were fabricated. The first set (M1) consisted of MSRI standard cell materials and was tested as the baseline. The second set (M2) was constructed with advanced cell materials to stabilize the electrolyzer performance. Based on the M2 cell results, the advanced cell materials were engineered further and the third set (M2<sup>+</sup>) of SOECs was thus fabricated and tested.

Non-stack components necessary for the SOEC stacks, including interconnects, seal gaskets, and electrode dry contact aids, were also machined.

#### **Task 2 – Construction and Testing of Two SOEC Stacks**

MSRI has successfully constructed and tested two stacks, each consisting of five planar SOECs for hydrogen production from steam. Figure 7-1 is a photograph of a typical 5-cell stack with voltage leads attached to individual cells. The stack dimension was about 5.5"x5.5"x0.5". Each stack was tested initially in the SOFC and SOEC modes for power generation and hydrogen production, respectively, followed by a long-term test in the SOEC mode with the stack current fixed at 14.3 amps. During tests,



Figure 7-1. Photograph of 5-cell SOEC stack.

polarization curves as a function of stack current were recorded at fixed utilizations of 40%. Voltage reading at each cell was also recorded and analyzed. The effect of negative electrode gas compositions was investigated by varying the hydrogen concentrations balanced with steam, which was generated by a vaporizer. A precision water pump was used to control the steam flow.

The first stack was constructed with five M1 cells which were made from MSRI's existing cell materials as the baseline. Figure 7-2 details the stack performance characteristics evaluated at 800°C in the SOFC mode with the hydrogen fuel concentrations varying from 100% to 50% balanced with steam. As shown in the figure, the effect of the negative electrode fuel compositions on the stack performance was negligible. At 20 amps, power outputs from this stack were ~74 W and 72 W for H<sub>2</sub> and 50%H<sub>2</sub> bal. H<sub>2</sub>O, respectively.

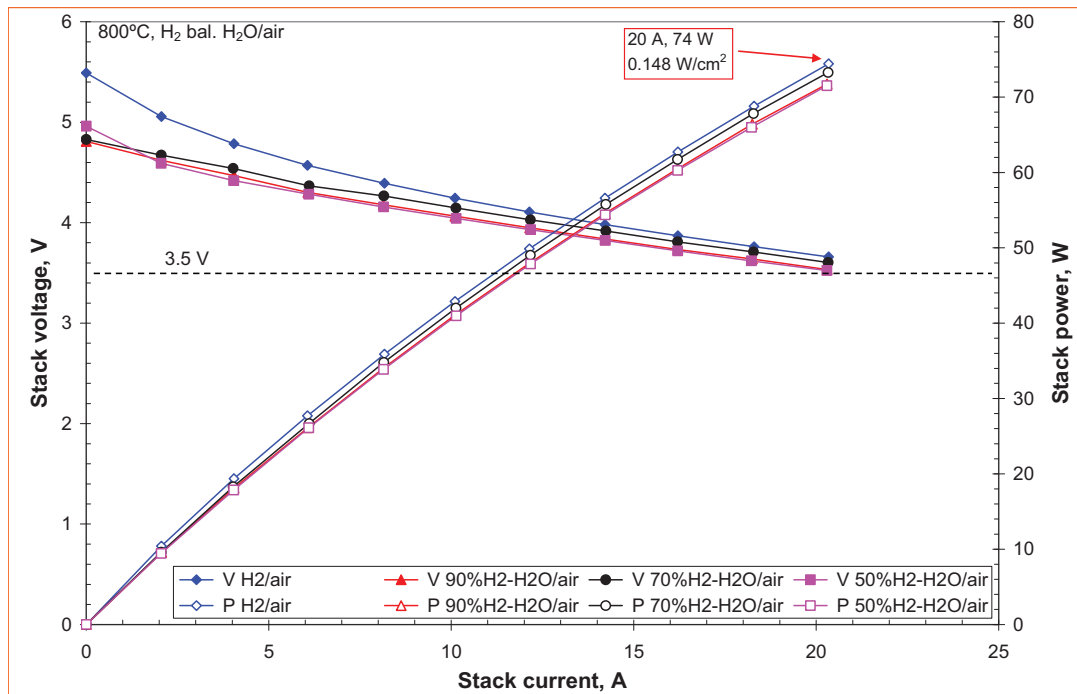


Figure 7-2. Performance characteristics of the M1 5-cell stack tested in the SOFC mode at 800°C. The compositions of the fuel gas were varied from H<sub>2</sub> to 50% H<sub>2</sub>, balance H<sub>2</sub>O.

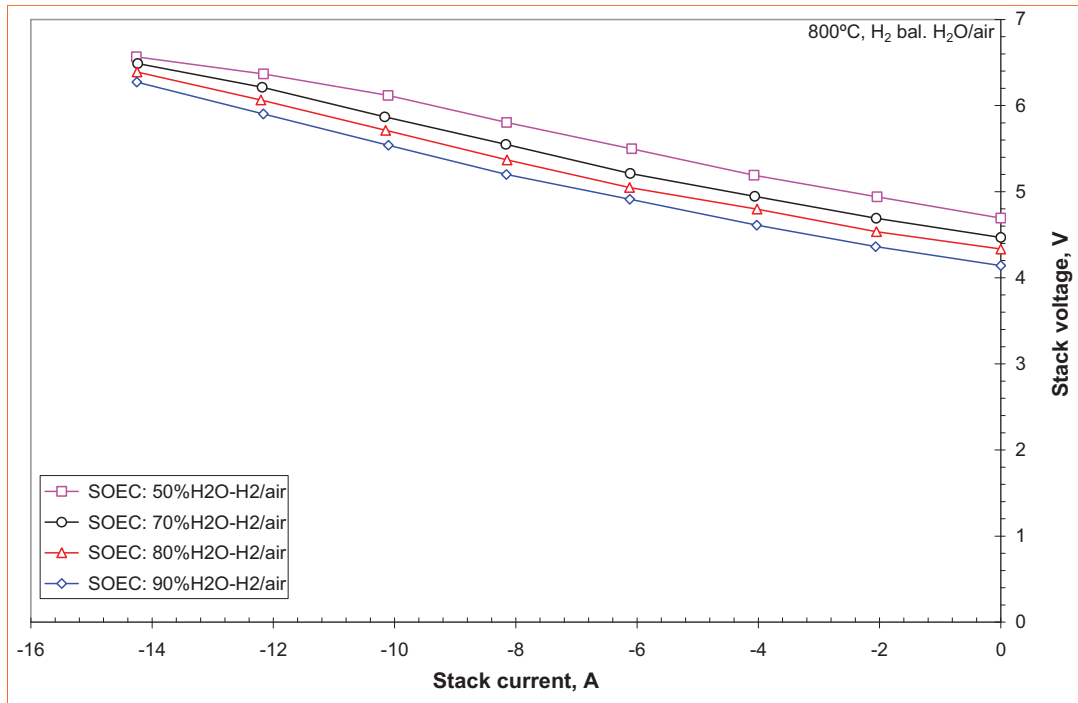


Figure 7-3. Performance characteristics of the same M1 5-cell stack tested in the SOEC mode at 800°C. The steam concentrations were varied from 90% to 50%.

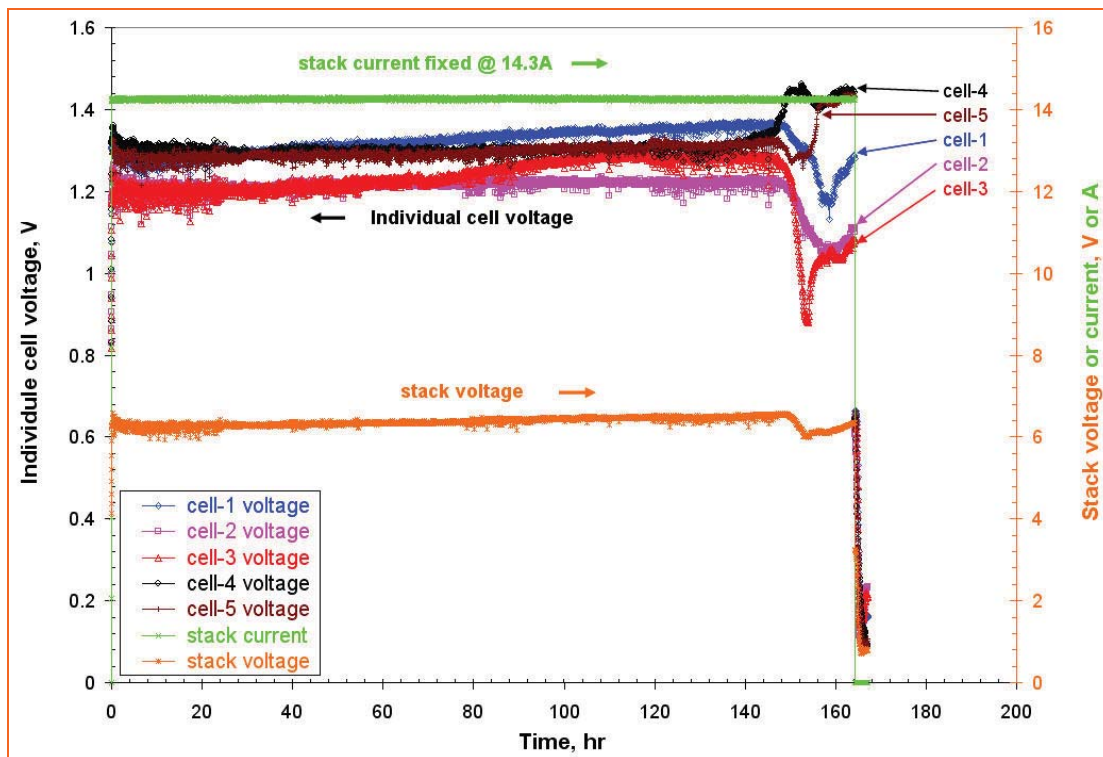


Figure 7-4. Long-term test result of the M1 5-cell stack in the SOEC mode at 800°C. The negative electrode gas was 90% H<sub>2</sub>O, balance H<sub>2</sub>.



After the SOFC baseline test, the same stack was tested in the SOEC mode for hydrogen production from steam. SOEC stack performance is shown in Figure 7-3 for various gas compositions on the negative electrode. At 14.3 amps, the stack consumed 90 W (at 6.3 V) and 94.4 W (at 6.6 V) electricity for the steam concentration of 90% and 50% bal. H<sub>2</sub>, respectively, for hydrogen production.

Immediately after the aforementioned SOFC and SOEC tests, the long-term test in the hydrogen production mode was carried out on the same day by setting the data recording time to zero. Figure 7-4 details the long-term test results at 800°C over 160 hours with 90% H<sub>2</sub>O, balance H<sub>2</sub> as the negative electrode gas. The stack current was fixed at 14.3 amps controlled by an external electronic load, and voltages of the stack and individual cells were recorded over time. As shown in the figure, the stack performance was nearly stable during the first 140 hours of continuous testing. However, it exhibited malfunction after 160 hours.

The second stack was constructed with five M2 cells consisting of advanced materials necessary to stabilize the electrolyzer performance. With the same testing procedure as the first stack, this M2 5-cell stack was tested in the SOFC and SOEC modes first, immediately followed by the long-term test in the hydrogen production mode. The test results are shown in Figure 7-5 through Figure 7-7. At 20 amps, this 5-cell stack generated 81 W and 76 W electricity for the H<sub>2</sub> fuel and 50% H<sub>2</sub> bal. H<sub>2</sub>O fuel, respectively. By comparing with the first stack performance shown in Figure 7-2, under the same operating conditions, the second stack performance was improved by nearly 9%. At 30 amps (or 0.3 A/cm<sup>2</sup>), the power density reached 0.22 W/cm<sup>2</sup>.

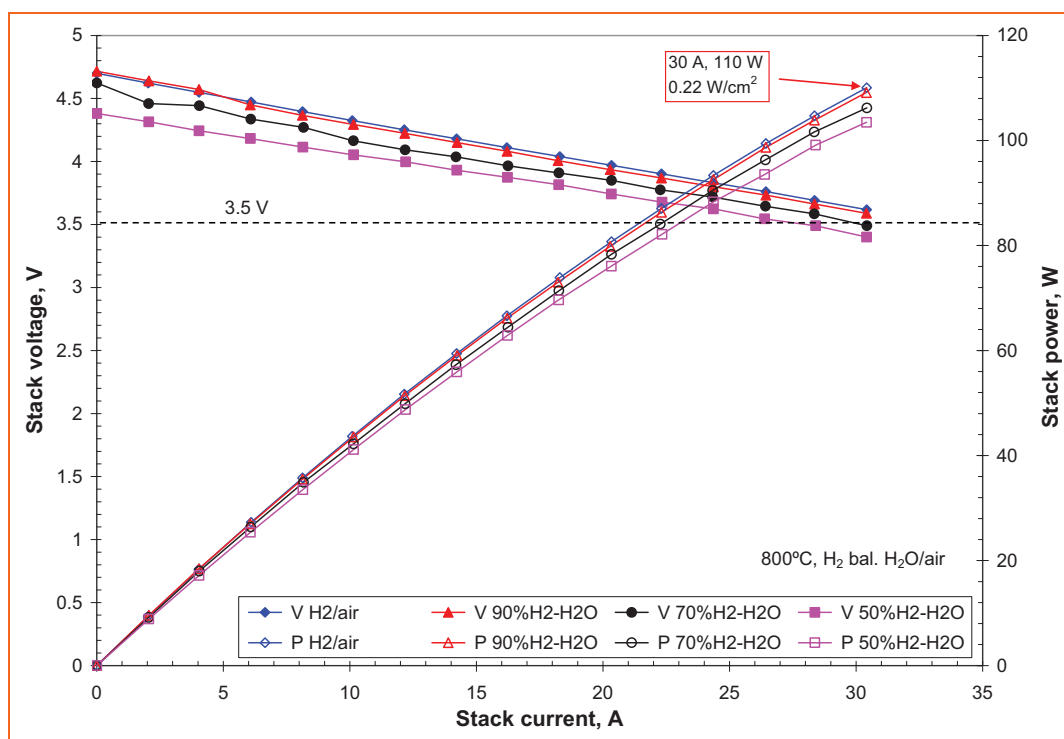


Figure 7-5. Performance characteristics of the M2 5-cell stack tested in the SOFC mode at 800°C. The compositions of the fuel gas were varied from H<sub>2</sub> to 50% H<sub>2</sub> bal. H<sub>2</sub>O.

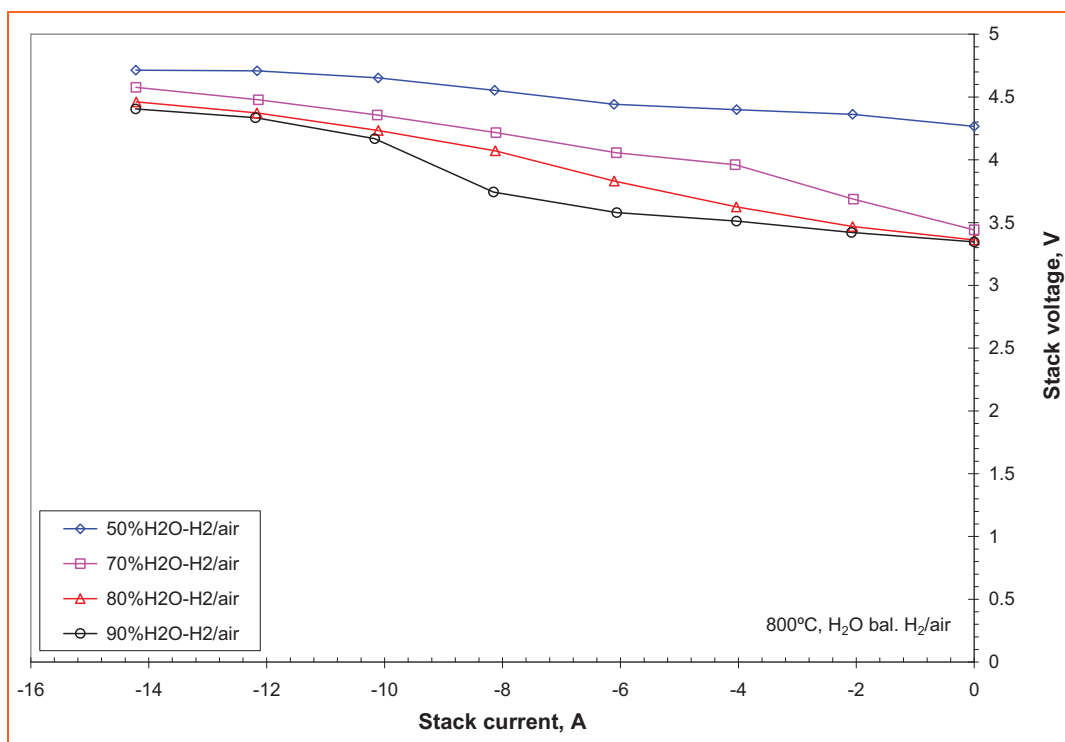


Figure 7-6. Performance characteristics of the same M2 5-cell stack tested in the SOEC mode at 800°C. The steam concentrations were varied from 90% to 50%.

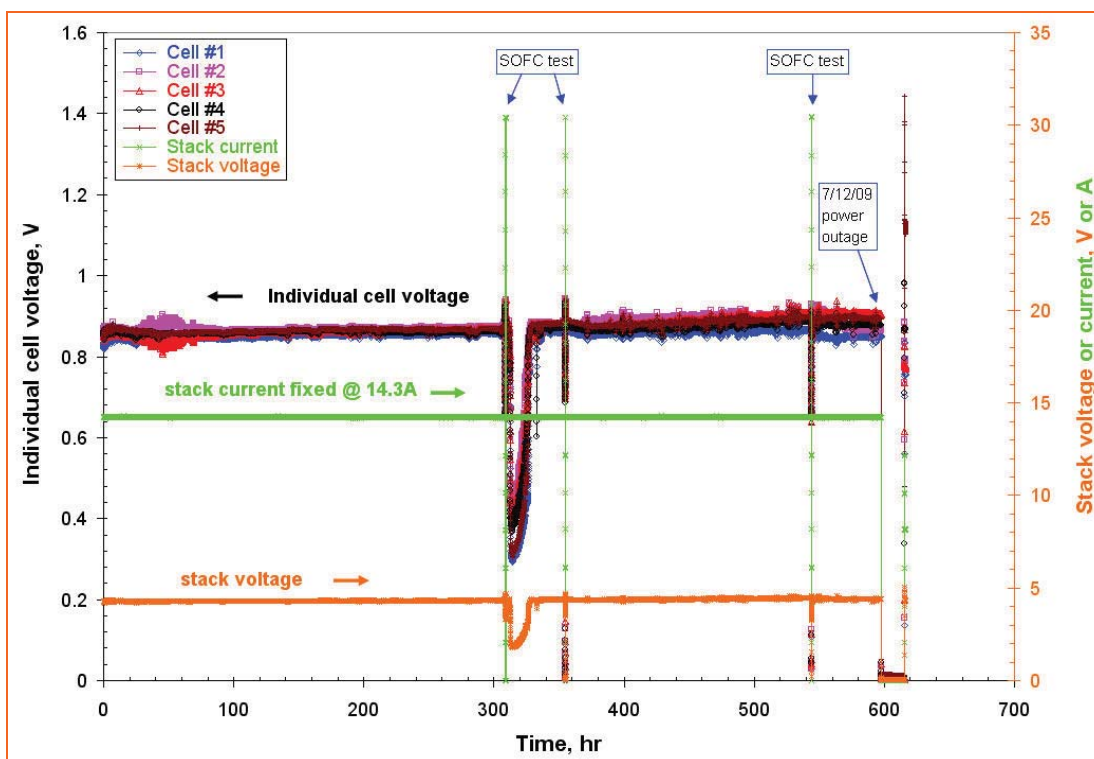


Figure 7-7. Long-term test result of the M2 5-cell stack in the SOEC mode for continuous hydrogen production at 800°C. The negative electrode gas was 70% $\text{H}_2\text{O}$  bal.  $\text{H}_2$ .

Figure 7-6 shows the stack performance characteristics tested in the SOEC mode with the steam concentrations varying from 50% to 90%, balance  $H_2$ . As shown in the figure, the power consumption was only 63 W at 14.3 amps, while the first stack needed 90 W power necessary for producing the same amount of hydrogen. It is equivalent to  $\sim 43\%$  performance improvement.

Figure 7-7 shows the long-term test results of the second stack with 70%  $H_2O$ , balance  $H_2$  as the negative electrode gas. This stack was tested over 610 hours with a constant current at 14.3 amps. As shown in the figure, the stack performance was very stable over the total testing during, particularly during the first 308 hours. Somehow, the stack exhibited malfunction after 309 hours, but was fully recovered after 330 hours.

The long-term test of continuous hydrogen production was interrupted for scheduled operations in the SOFC mode for power generation, which served as check-points for the functionality of the stack. Figure 7-8 shows the stack SOFC performance tested at different time. In these tests, 50%  $H_2$ , balance  $N_2$  was the fuel and air was the oxidant. The first SOFC point-check was performed after 308 hours. It was interesting to note that the stack showed a malfunction right after the stack was switched back to the long-term test from the first point-check. Furthermore, the stack performance of the second check-point after 355 hours was nearly as good as the initial performance, indicating a full recovery from the malfunction. The third check-point was performed after 544 hours with the stack performance decreased by 10% from the initial performance. Postmortem analyses were performed and results will be discussed in Task 4.

To date, two stacks have been constructed, one using MSRI standard materials and the second using advanced cell materials. Long-term tests of both stacks were performed successfully over extended hours, and greatly exceeded the project targets. During both tests, communication between MSRI and BEA/INL was well maintained, and the stack performances were reviewed by BEA/INL personnel who

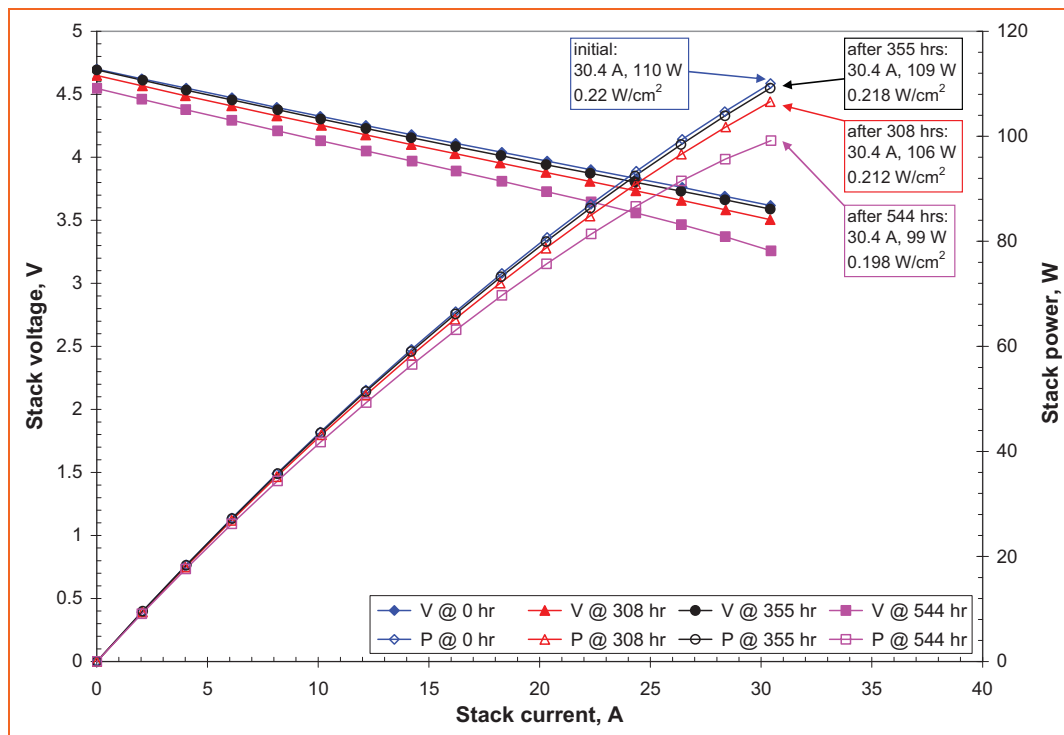


Figure 7-8. M2 5-cell stack functional checks in the SOFC mode at different time. 50% $H_2$  bal.  $N_2$  was the fuel and air was the oxidant. All tests were performed at 800°C.

also visited MSRI to observe the tests of the second stack. As discussed above, the M2 stack with the advanced cell materials showed much improvement in both stack initial performance and stability. The M2 cells were designed to be operated at a relatively low voltage, as shown in Figure 7-6. With full consent of BEA/INL personnel, MSRI initiated further advanced materials improvement, which will be discussed in Task 3 below.

### Task 3 – Fabrication and Testing of the Third SOEC Stack

After completing the second test, the advanced materials for M2 cells were reevaluated and engineered for performance improvement. With the BEA/INL personnel's authorization, MSRI fabricated and tested the third stack with five M2<sup>+</sup> cells. Similar to the previous tests of two stacks, the third stack was tested in the SOFC and SOEC modes first, followed by the long-term test in the hydrogen production mode. Scheduled tests in the SOFC mode were also performed during the long-term test as check-points of the stack functionality at different times. Test results are shown in Figure 7-9 through Figure 7-12. Compared to the second stack, the effectiveness of improvement in stack performance and open circuit voltages was evident, as shown in Figure 7-9 and Figure 7-10.

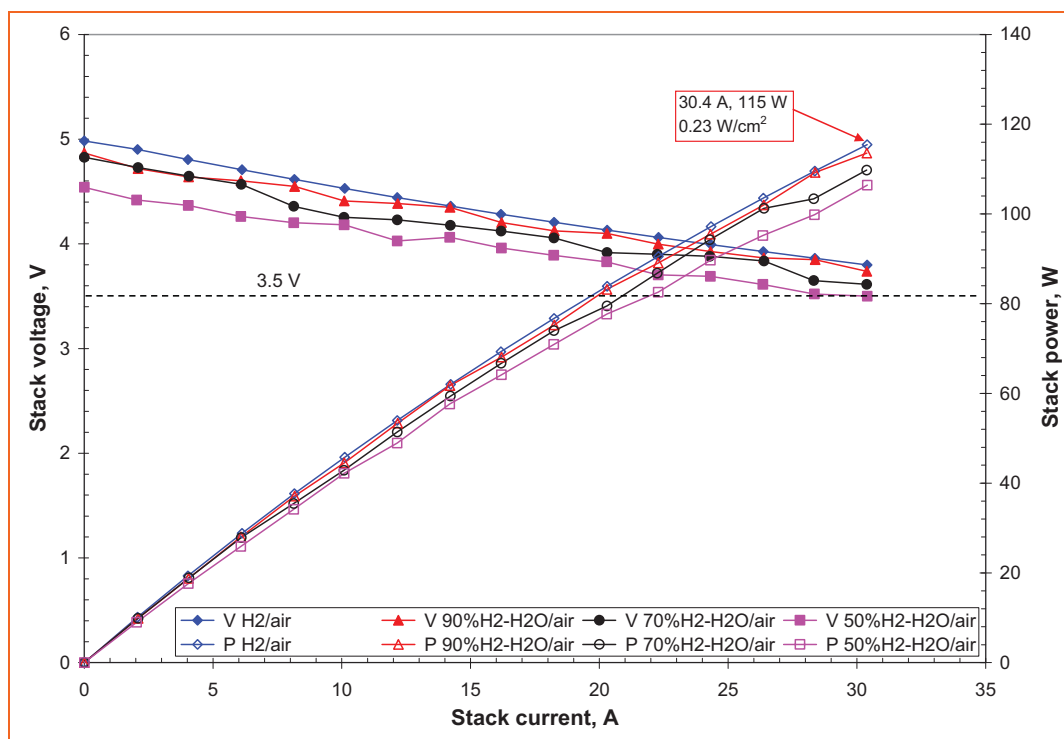


Figure 7-9. Performance characteristics of the M2<sup>+</sup> 5-cell stack tested in the SOFC mode at 800°C. The compositions of the fuel gas were varied from H<sub>2</sub> to 50% H<sub>2</sub>, balance H<sub>2</sub>O.

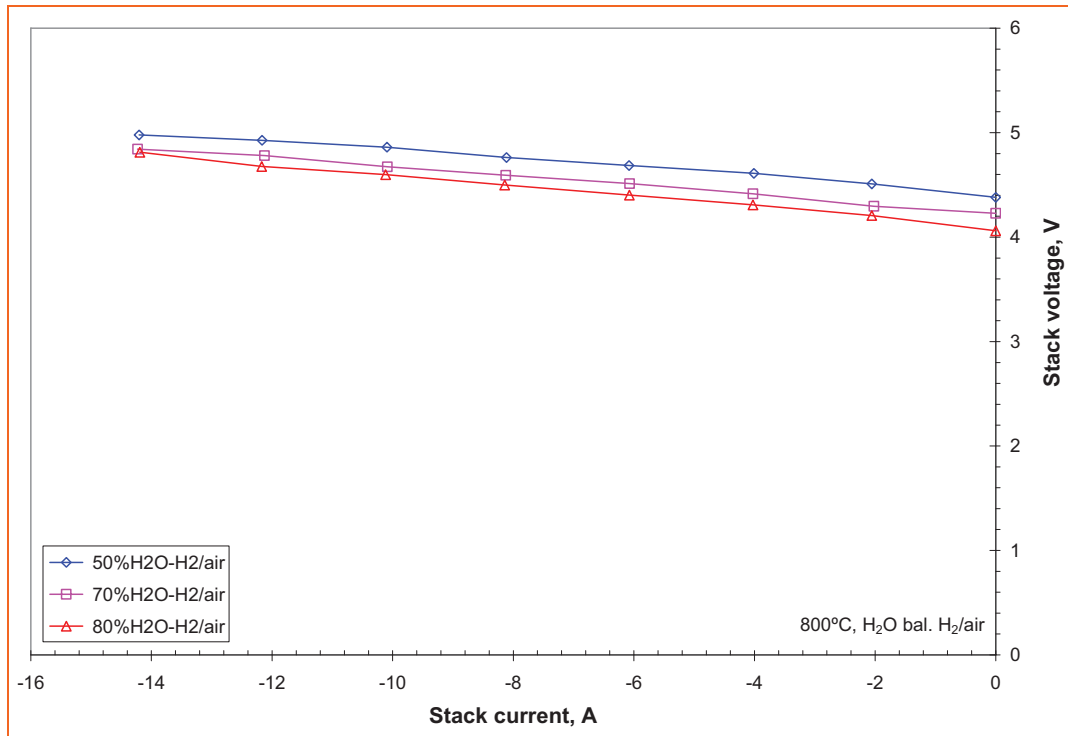


Figure 7-10. Performance characteristics of the same M2<sup>+</sup> 5-cell stack tested in the SOEC mode at 800°C. The steam concentrations were varied from 80% to 50%.

Figure 7-11 details the long-term test results of the M2<sup>+</sup> 5-cell stack with 70% H<sub>2</sub>O bal. H<sub>2</sub> as the negative electrode gas. This stack was tested over 815 hours with a constant current at 14.3 amps. As shown in the figure, the stack performance was fairly stable. Due to the monsoon season, during the long-term test the stack suffered five unexpected power outages on 07/12, 07/21, 07/28, 08/03, and 08/05, all during nights. In addition, the long-term test was also interrupted four times for scheduled SOFC tests for power generation. The SOFC performance at different time is shown in Figure 7-12. Nearly no degradation was observed over the first 459 hours. The last check-point was performed after 651 hours, and it exhibited ~6% performance degradation comparing with the initial performance.

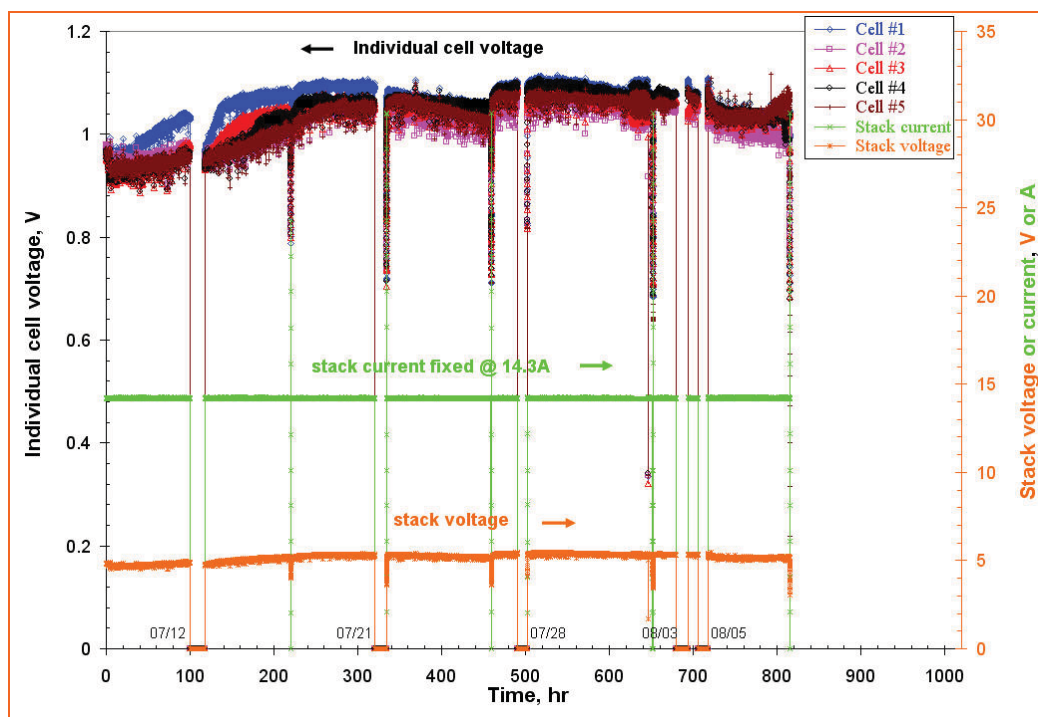


Figure 7-11. Long-term test result of the M2<sup>+</sup> 5-cell stack in the SOEC mode for a continuous hydrogen production at 800°C. The negative electrode gas was 70%H<sub>2</sub>O bal. H<sub>2</sub>.

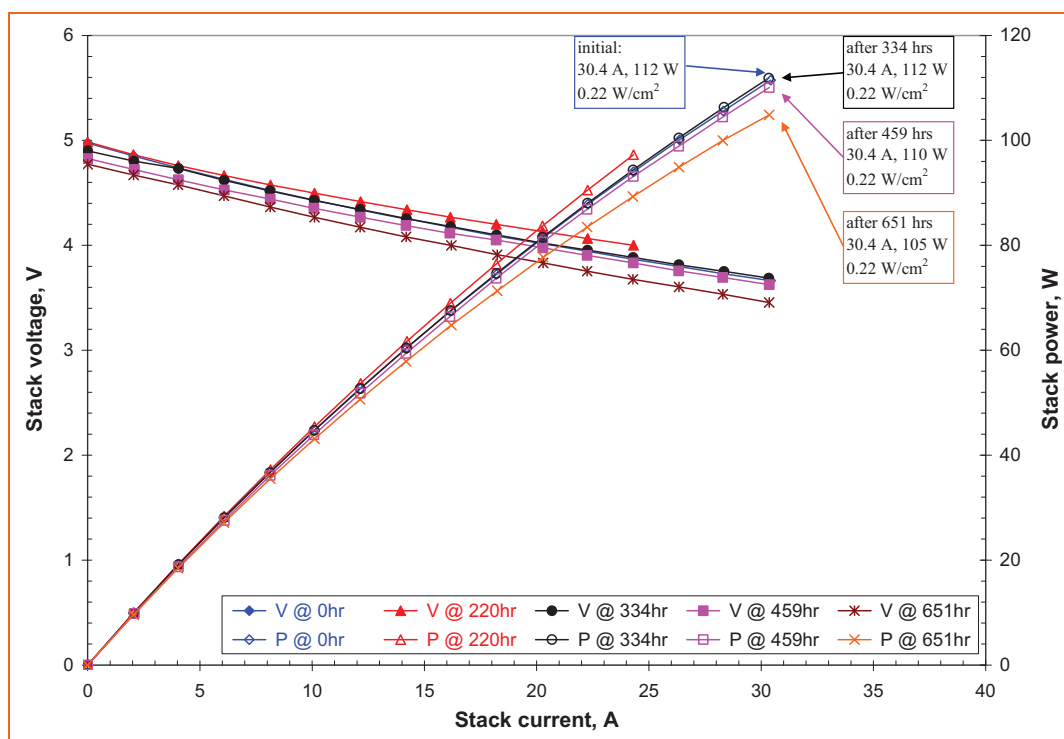


Figure 7-12. M2<sup>+</sup> 5-cell stack functional check in the SOFC mode at different time. 50%H<sub>2</sub> bal. N<sub>2</sub> was the fuel, and air was the oxidant. All tests were performed at 800°C.



The long-term test was terminated after 815 hours, which also significantly exceeded the project target at 200 hours. During the test, BEA/INL personnel visited MSRI to observe the tests.

#### Task 4 – Post Test Analysis

After completing the first two tests, stacks were inspected visually before being moved out of the furnace. Any signs of cracks were recorded. Figure 7-13 are the photographs of the test fixture used for the second stack (M2) long-term tests over 610 hours. As highlighted in the photos, the inlet tube for the negative electrode gas was corroded, leading to the stack operating in steam starvation condition during the tests. The tube fell apart after the test fixture was moved out of the furnace.

Two stacks were disassembled, and individual cells were marked and examined for any signs of physical damage or delamination. Selected cells were cut along the cross-section and examined with scanning electron microscopy (SEM). Figure 7-14 (a) and (b) are the SEM micrographs of typical post-test cells of a M1 cell and a M2 cell, respectively. No apparent electrode delaminations were observed.

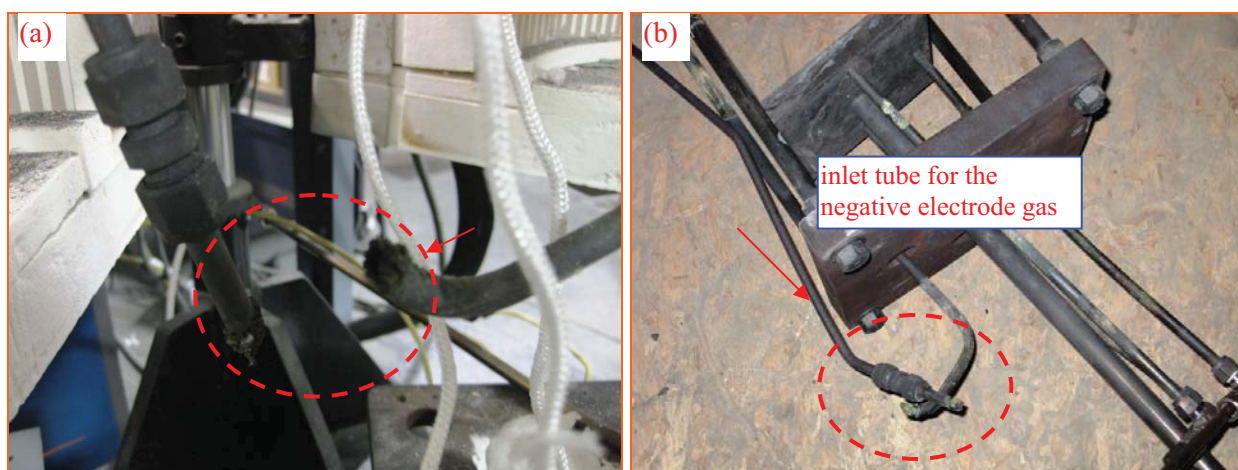


Figure 7-13. Photographs of the test fixture after long-term tests of the second 5-cell stack: (a) before and (b) after moved out of the furnace.

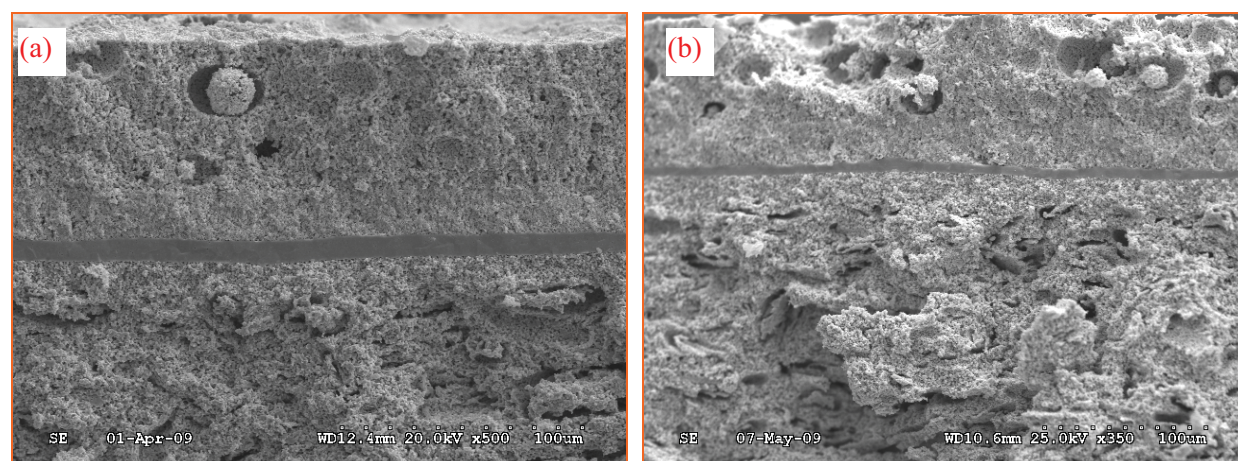


Figure 7-14. SEM micrographs of (a) a M1 cell with MSRI standard cell materials; (b) a M2 cell with the advanced cell materials, after long-term tests.

## **8. ACKNOWLEDGMENTS**

This work was supported by the U.S. Department of Energy, Office of Nuclear Energy, Nuclear Hydrogen Initiative Program. The Idaho National Laboratory is operated for the U.S. Department of Energy's Office of Nuclear Energy by the Battelle Energy Alliance under contract number DE-AC07-05ID14517.



## 9. REFERENCES

- Akkaya, A. V., 2007, "Electrochemical Model for Performance Analysis of a Tubular SOFC," *Int. J. Energy Research*, 31, 79–98.
- Carter, D. J. et al., 2008, "Determining Causes of Degradation in High Temperature Electrolysis Stacks," *Workshop on Degradation in Solid Oxide Electrolysis Cells and Strategies for its Mitigation, Fuel Cell Seminar & Exposition, Phoenix, AZ, October 27, 2008*.
- Gazzarri, J. I., 2007, "Impedance Model of a Solid Oxide Fuel Cell for Degradation Diagnosis," Ph. D. Thesis, University of British Columbia, Vancouver, Canada.
- Gemmen, R. S., Williams, M. C., and Gerdes, K., 2008, "Degradation Measurement and Analysis for Cells and Stacks," *J. Power Sources*, 184, 251–259.
- Guan, J. et al., 2006, "High Performance Flexible Reversible Solid Oxide Fuel Cell," *GE Global Research Center Final Report for DOE Cooperative Agreement DE-FC36-04GO-14351*.
- Haering, C., Roosen, A., Schichl, H., and Schnoller, M., 2005, "Degradation of the electrical conductivity in stabilized zirconia system Part II: Scandia-stabilised zirconia," *Solid State Ionics*, 176, 3–4, 261–268.
- Hartvigsen, J. J., Larson, D., and Elangovan, S., 2009, "Post Test Stack Disassembly of Stacks A and B from Module #3 from the Full Scale ILS Test in the 4<sup>th</sup> Quarter 2008," Ceramartec Progress Report to INL for Subcontract 83664.
- Hauch, A., 2007a, "Solid Oxide Electrolysis Cells – Performance and Durability," Ph.D. Thesis, Technical University of Denmark, Risø National Laboratory, Roskilde, Denmark.
- Herring, J. S., Stoots, C. M., O'Brien, J. E., Hartvigsen, J. J., and Housley, G., 2007, "Recent Progress in High Temperature Electrolysis," AICHE Meeting, Salt Lake City, UT, November 5–9, 2007.
- Ivers-Tiffée, E. and Virkar, A. V., 2003, "Electrode Polarisation," Chapter 9 in *High Temperature Solid Oxide Fuel Cells: Fundamentals, Design and Applications*, Edited by Singhal, S. C. and Kendall, K., Elsevier, Oxford, U.K.
- Ni, M., Leung, M. K. H., and Leung, D. Y. C., 2006, "A Modeling Study on Concentration Overpotentials of a Reversible Solid Oxide Fuel Cell," *J. Power Sources*, 163, 460–466.
- O'Brien, J. E., Stoots, C. M., Herring, J. S., and Hartvigsen, J. J., 2007, "Performance of Planar High-Temperature Electrolysis Stacks for Hydrogen Production from Nuclear Energy," *Nuclear Technology*, 158, 118–131.
- O'Brien, J. E., Stoots, C. M., Herring, J. S., Condie, K. G., and Housley, G. K., 2009a, "The High-Temperature Electrolysis Program at the Idaho National Laboratory: Observations on Performance Degradation," High Temperature Water Electrolysis Limiting Factors, Eifer, Karlsruhe, Germany, June 9–10, 2009.
- O'Brien, J. E., McKellar, M. G., Harvego, E. A., and Stoots, C. M., 2009b, "High-Temperature Electrolysis for Large-Scale Hydrogen and Syngas Production from Nuclear Energy – system Simulation and Economics," International Conference on Hydrogen Production, ICH2P-09, Oshawa, Canada, May 3–6, 2009.
- Sohal, M. S., 2009a, "Degradation in Solid Oxide Cells during High Temperature Electrolysis," Idaho National Laboratory Report INL/EXT-09-15617.
- Sohal, M. S., O'Brien, J. E., Stoots, C. M., Herring, J. S., Hartvigsen, J. J., Larsen, D., Elangovan, S., Carter, J. D., Sharma, V. I., and Yildiz, B., 2009b, "Critical Causes of Degradation in Integrated

Laboratory Scale Cells during High-Temperature Electrolysis,” Idaho National Laboratory Report INL/EXT-09-16004.

Stoots, C. M., Condie, K. G., O’Brien, J. E., and Housley, G., 2009a, “Integrated Laboratory Scale Test Report,” Idaho National Laboratory Report INL/EXT-09-15283.

Virkar, A. V., 2007, “A Model for Solid Oxide Fuel Cell (SOFC) Stack Degradation,” *J. Power Sources*, 172, 713–724.

Windisch, C. F., Stevenson, J. W., Simner, S. P., Williford, R. E., and Chick, L. A., 2002, “Experimentally-Calibrated Spreadsheet-based SOFC Unit-Cell Performance Model,” Pacific Northwest National Laboratory, PNNL-SA-37014, presented at *2002 Fuel Cell Seminar: Fuel Cells-Reliable, Clean Energy for the World, Palm Springs, CA, November 21, 2002*.